Clim Dyn (2013) 40:775–803
DOI 10.1007/s00382-012-1412-2

An assessment of oceanic variability for 1960–2010 from the GFDL ensemble coupled data assimilation

You-Soon Chang · Shaoqing Zhang · Anthony Rosati · Thomas L. Delworth · William F. Stern

Received: 4 November 2011 / Accepted: 28 May 2012 / Published online: 16 June 2012

Abstract The Geophysical Fluid Dynamics Laboratory has developed an ensemble coupled data assimilation (ECDA) system based on the fully coupled climate model, CM2.1, in order to provide reanalyzed coupled initial conditions that are balanced with the climate prediction model. Here, we conduct a comprehensive assessment for the oceanic variability from the latest version of the ECDA analyzed for 51 years, 1960–2010. Meridional oceanic heat transport, net ocean surface heat flux, wind stress, sea surface height, top 300 m heat content, tropical temperature, salinity and currents are compared with various in situ observations and reanalyses by employing similar configurations with the assessment of the NCEP's climate forecast system reanalysis (Xue et al. in Clim Dyn 37(11): 2511–2539, 2011). Results show that the ECDA agrees well with observations in both climatology and variability for 51 years. For the simulation of the Tropical Atlantic Ocean and global salinity variability, the ECDA shows a good performance compared to existing reanalyses. The ECDA also shows no significant drift in the deep ocean temperature and salinity. While systematic model biases are mostly corrected with the coupled data assimilation, some biases (e.g., strong trade winds, weak westerly winds and warm SST in the southern oceans, subsurface temperature and salinity biases along the equatorial western Pacific boundary, overestimating the mixed layer depth around the subpolar Atlantic and high-latitude southern oceans in the winter seasons) are not completely eliminated. Mean biases such as strong South Equatorial Current, weak Equatorial Under Current, and weak Atlantic overturning transport are generated during the assimilation procedure, but their variabilities are well simulated. In terms of climate variability, the ECDA provides good simulations of the dominant oceanic signals associated with El Nino and Southern Oscillation, Indian Ocean Dipole, Pacific Decadal Oscillation, and Atlantic Meridional Overturning Circulation during the whole analyzed period, 1960–2010.

Keywords Ensemble coupled data assimilation · Reanalysis · Assessment · Oceanic variability

Y.-S. Chang (✉) · S. Zhang · A. Rosati · T. L. Delworth · W. F. Stern
Geophysical Fluid Dynamics Laboratory, Princeton University Forrestal Campus, 201 Forrestal Road, Princeton, NJ 08540, USA
e-mail: You-Soon.Chang@noaa.gov

Y.-S. Chang
University Corporation for Atmospheric Research, Boulder, CO, USA

1 Introduction

The skill of climate prediction is subject to a variety of errors arising primarily from poorly determined oceanic initial conditions, coupled model errors and the unpredictability of synoptic atmospheric variability. Among them, accurate oceanic initialization plays a critical role since most of predictability on seasonal to decadal time scales comes from the ocean memory (Smith et al. 2007). However, in most existing operational systems, ocean initialization is still done in an uncoupled way and there is little attempt to obtain ocean initial conditions that are balanced within the coupled system. A common approach for initialization of the ocean component for a coupled climate forecast system is to assimilate only ocean observations into a separate ocean model forced by prescribed atmospheric fluxes, which often results in initialization

shocks that may degrade the model's forecast skill (Schneider et al. 1999). Therefore, several groups are currently trying to develop an advanced data assimilation technique to impose well balanced constraints between the ocean state and the coupled model, or exploring alternative strategies to avoid initialization shock.

Sugiura et al. (2008) demonstrated that their four-dimensional variation coupled data assimilation system has the ability to enhance forecast potential for seasonal to interannual phenomena. Yang et al. (2009) investigated the potential applications of bred vectors generated from the NASA Global Modeling and Assimilation Office (GMAO) coupled general circulation model (CGCM). They showed that bred vectors improve ensemble mean SST forecasts and capture information on flow-dependent uncertainty that can be used for background error covariance in ocean assimilation. At the National Centers for Environmental Prediction (NCEP), a new partially coupled ocean and atmosphere data assimilation system, referred to as the climate forecast system reanalysis (CFSR), was developed and completed the reanalysis of the atmosphere, ocean, sea ice and land for 1979–2009 (Saha et al. 2010). The Geophysical Fluid Dynamics Laboratory (GFDL) had been also involved in the project on a coupled initialization process and developed a state-of-the-art ensemble coupled data assimilation (ECDA) system. Zhang et al. (2007) described the advantage of the coupled data assimilation approach and the ECDA system structure in detail. Several assimilation experiments were carried out with specified oceanic and atmospheric variables (ocean data assimilation with subsurface temperature and salinity (T–S), atmospheric data assimilation with air temperature and wind, and coupled data assimilation) and evaluated by a twin experiment. With a similar method, an adaptively-inflated ensemble filter algorithm has been evaluated (Zhang and Rosati 2010). Chang et al. (2011b) also showed additional improvements of salinity representation in the ECDA with independent Argo data. To improve our understanding of climate change by using the ECDA, Zhang et al. (2009) investigated the impact of observing systems, external radiative forcings and initial conditions on the detection of long time variability of oceanic heat content and salinity. They also carried out similar study focusing on monitoring the Atlantic Meridional Overturning Circulation (AMOC) and associated North Atlantic climate (Zhang et al. 2010). After a couple of improvements from previous studies as we introduced, our ECDA system completed ocean reanalysis from 1960 to present. Data can be found at http://www.gfdl.noaa.gov/ocean-data-assimilation.

The main purpose of this study is to inform the user community about the general features in the ECDA ocean component, and how the ocean reanalysis from the fully coupled assimilation model compares with in situ observations. With the similar purpose, Xue et al. (2011) (hereafter referred to as X11) published a comprehensive evaluation of the results for the oceanic variability in the NCEP's CFSR, so we intentionally follow their configuration by selecting similar model variables, study areas, and observed datasets. We expect that this collocated configuration leads to an additional comparison between the ECDA and CFSR. Moreover, in this study, we include meridional heat transport and Atlantic overturning features simulated by the ECDA and extend the analyzed period from 1960 to 2010. Analyzed period over 50 years is quite a challenge when we consider the non-stationary nature of the ocean observing system especially for the twentieth century.

The following section provides a detailed description of the model, assimilation scheme, and ocean observations used in the ECDA system. Section 3 shows the results of the validation of the ECDA by using various in situ observational and analyzed datasets around various areas. In this section, we also assess the dominant modes associated with four major climate variabilities (El Nino and Southern Oscillation (ENSO), Indian Ocean Dipole (IOD), Pacific Decadal Oscillation (PDO), and AMOC). The summary and conclusion appear in Sect. 4.

2 ECDA system

2.1 Model

The GFDL ECDA system employs an ensemble-based filtering algorithm applied to the GFDL's fully coupled climate model, CM2.1, which is one of two GFDL IPCC AR4 models (Delworth et al. 2006). The atmosphere/Land model (AM2.1/LM2.1) is based on a finite-volume dynamic core (Lin 2004) and has 2.5° longitude by 2° latitude horizontal resolution and 24 vertical levels. The physics package includes a K-profile planetary boundary layer (Lock et al. 2000), relaxed Arakawa-Schubert convection (Moorthi and Suarez 1992) and a simple local parameterization of the vertical momentum transport by cumulus convection. The ocean model (MOM4) is configured with 1° by 1° horizontal resolution telescoping to 1/3° meridional spacing near the equator and 50 vertical levels (22 levels of 10 m thickness in the top 220 m). The model has an explicit free surface with a freshwater flux exchange between the atmosphere and ocean. K-profile parameterization vertical mixing, neutral physics, a spatially-dependent anisotropic viscosity, and a shortwave radiative penetration depth that depends on a prescribed climatological ocean color are parameterized. Insolation varies diurnally and the wind stress at the ocean surface is computed using the velocity of the wind relative to the

surface currents. An efficient time-stepping scheme is also employed. More details can be found in Griffies et al. (2005) and Gnanadesikan et al. (2006). The Sea Ice Simulator in the coupled model is a dynamical ice model with three vertical layers (one for snow and two for ice) and five ice-thickness categories. The elastic-viscous-plastic technique (Hunke and Dukowicz 1997) is used to calculate ice internal stress, and the thermodynamics is a modified Semtner three-layer scheme (Winton 2000). The coupled components of this model interact with each other throughout the flux exchange.

2.2 Data assimilation scheme

The assimilation module of CM2.1 estimates the probability distribution function (PDF) of climate states by combining the prior PDF derived from coupled model dynamics and the observational PDF. It uses a two-step data assimilation procedure (the first step computes ensemble increments at an observation location and the second step distributes the increments over the impacted grids) for an ensemble Kalman filter under a local least squares framework with super-parallelized technique. The filtering process is implemented by a multivariate linear regression with careful consideration of temperature and salinity covariance (Anderson 2003). The data-adjusted ensemble members are the realizations of the analysis PDF and serve as the initial conditions for the next ensemble integration. Their analysis steps are performed daily. The ensemble data assimilation is tested using 6, 12 and 24 members and no significant improvement is found from 12 members to 24 members. Based on the test results, all ECDA experiments are performed with a 12-member ensemble that is used to compute state estimation (ensemble mean) and the spread of the estimate. The ECDA also uses an adaptively-inflated ensemble filter that is designed to enhance the consistency of upper and deep ocean adjustments, based on climatological standard deviation being adaptively updated by observations. A first guess of climatological standard deviation is estimated using a long time series of anomalies in a simulation of the assimilation model. This standard deviation is updated by the assimilation product every year to inflate the prior ensemble in the filtering. This new algorithm coherently increases data constraints in the deep ocean based on the climatological variance of appropriate vertical localization scales. More details on the algorithm and parameter scales can be found at Zhang and Rosati (2010). As we previously mentioned, this fully coupled model methodology is chosen to produce a balanced state between the state variables of the atmosphere and ocean.

2.3 The ocean observations

Ocean subsurface observations of temperature, salinity, and SST are assimilated to the ECDA system using covariance structures from the coupled model where the atmosphere is constrained by an existing atmospheric reanalyses [NCEP/NCAR reanalysis 1 for 1960–1978 (Kalnay et al. 1996) and NCEP/DOE reanalysis 2 for 1979–2010 (Kanamitsu et al. 2002)]. Three atmospheric variables (air temperature, u, and v) from 6-h mean NCEP reanalyses (full grid points) are chosen as the observations to be assimilated in the ECDA. The correlation scales employed in the atmospheres filtering analysis are 1,000 km for temperature and 500 km for u and v, respectively (details can be found at section 5. "Test on ADA" from Zhang et al. 2007).

Subsurface ocean temperature and salinity observations basically include 5 types of oceanic profiles (XBT, CTD, OSD, MBT, and MRB) from World Ocean Database 2009 (WOD09) (Boyer et al. 2009). Since subsurface salinity observations were extremely sparse prior to Argo period, Chang et al. (2011a) constructed so-called pseudo salinity profiles from the weighted least square procedure that minimizes the misfits between the predetermined vertical coupled T–S EOF modes and the observed temperature and altimetry data. These pseudo salinity profiles are assimilated to the ECDA for the periods of 1993–2002. An important advantage of this approach is that it significantly reduces the salinity mean bias of the coupled model and maintains an interannual variability (Chang et al. 2011b). The altimetry sea surface height (SSH) information is partially used for the generation of pseudo salinity profiles, but not directly assimilated to the current ECDA system. It will be included in the ECDA system at a later stage.

Since 2000, we have added the PFL (autonomous profiling Argo floats) type data to our ECDA system. Because Argo data should be used with higher quality delayed mode, we constructed another data-mirroring system from the Argo global data assembly center (GDAC) in charge of the global Argo data distribution in near real time with a full salinity accuracy and quality control (QC) flag. The Argo QC system used for the ECDA considers not only the conventional QC process based on the National Oceanographic Data Center (NODC) technical report and Argo real time QC manual, but also any systematic instrument errors such as Argo salinity offsets identified from delayed mode QC methods and pressure sensor errors discovered in some fractions of the floats with FSI (Falmouth Scientific, Inc.) and SBE (SeaBird Electronics, Inc.) sensors (Chang et al. 2009). Any systematic bias associated with fall rate equation problem of XBT (Gouretski and Kiltermann 2007) has been also considered in the ECDA. Several new XBT correction methods have been suggested (Wijffels et al. 2008; Levitus et al. 2009; Ishii and Kimoto 2009; Gouretski and Reseghetti 2010), but no agreement has been made for the official method. The bias adjustment associated with fall-rate equation is an area of current study, and may change in the future. Therefore, NODC also applied

their adjustment (Levitus et al. 2009) only to the "standard depth" datasets (http://www.nodc.noaa.gov/OC5/WOD09/bt_bias_notes.html). The ECDA used "observed full depth" data, so we obtained the XBT drop rate information from on the "depth-fix" flag of the WOD09 and corrected them based on Hanawa et al. (1995) and Kizu et al. (2005).

The ECDA covers the periods from 1960 to present and is being updated monthly, so we have used the global temperature–salinity profile program (GTSPP) datasets (http://www.nodc.noaa.gov/GTSPP/gtspp-home.html) since 2009 when the WOD09 is not covered. GTSPP has assembled and distributed the up-to-date global temperature and salinity data transmitted by the global telecommunication system (GTS) in near real time. For the ECDA system, we used "best-copy" data from the GTSPP continuously managed database (CMD). This "best-copy" data file replaces the real time low resolution (accuracy) one when NODC provides the full resolution, or fully processed and QC data. In order to avoid any data redundancy between Argo and GTSPP, we identified all PFL types from the mixed GTSPP datasets and then replaced them with our own Argo datasets being updated every month as well.

For the SST, NOAA optimum interpolation (OI) SST v2 analysis is used. They are produced weekly on a 1° grid available since November 1981. This analysis uses in situ and satellite SSTs plus SSTs simulated by sea ice cover. Before the analysis is computed, the satellite data is adjusted for biases using the method of Reynolds et al. (2002). Prior to November 1981 when OI SST is not available, we just used HadISST (Rayner et al. 2003). Since June 2002, it has been available to use quarter degree daily mean AMSR + AVHRR OISST version (Reynolds and Chelton 2010). This version guarantees a faster chain of data acquisition for the operational forecasting system as well as better resolution for the ECDA based on high resolution coupled model (CM2.5) in the near future (Delworth et al. 2012).

In situ observational and analyzed datasets for the validation of the ECDA for 51 years are similar with the companion paper (X11) and will be mentioned at the next sections together with verification results.

3 Results

3.1 Ocean heat transport

The meridional heat transport (MHT) by the oceans is an important factor in the ability of models to simulate realistic climate. The total simulated MHT by the ocean, as well as previous estimations based on observations, are shown in Fig. 1. For the entire globe, there appears to be insufficient northward (southward) transport of heat out of the Tropics in the ECDA, compared to observations around 24°N and 35°N (19°S). These general discrepancies in the northern (southern) hemisphere are mostly apparent in the Atlantic (Indo-Pacific) Ocean. For the twentieth century simulation, most of simulated MHT are in agreement with observational estimates within the error bounds (see yellow, green, and blue lines in Fig. 1), because previous studies estimated the MHT based on short-term observations in the twentieth century. The substantial uncertainty of existing estimations and the lack of long-term sustained observations make it difficult to assess the MHT variability of the ECDA for 51 years including twenty-first century.

Interestingly, the MHT from the ECDA depicts large variability on annual to decadal time scales for 51 years. Northward heat transport from the Tropics is getting smaller in time especially around 10°N–30°N. This tendency is generally shown for the global ocean including both Atlantic and Indo-Pacific Ocean. In particular, Atlantic MHT during 2000–2010 (red line in Fig. 1b) is much smaller than ones during the twentieth century, even though it is still consistent with the observational estimate of 0.73 ± 0.2 PW at 8°N (Talley 2003). This rapid change may be related to the spin up period of the Argo array up to 2,000 m which is assimilated to the ECDA system, but a clear understanding is not made from this study. The purpose of this manuscript is not to analyze the heat transport change around individual ocean basins in detail, but to show the general features of the newly developed ocean reanalysis for 51 years. Therefore, we expect that detailed investigation of the decadal MHT change especially between pre- and post-Argo period around the Atlantic Ocean will be followed in future studies.

3.2 Surface heat fluxes and wind stress

Yu and Weller (2007) generated the objectively analyzed latent and sensible heat fluxes (OAFlux) and validated them against in situ buoy observations. They provided the accuracy rates about 9.6 W/m^2 for latent heat flux and 2.6 W/m^2 for sensible heat flux, respectively. Gridded net sea surface shortwave and longwave radiation datasets can be also obtained from the International Satellite Cloud Climatology Project (ISCCP) (Zhang et al. 2004). We estimate the net ocean surface heat flux combined by OAFlux and ISCCP fluxes and compare it with the ECDA results for 1984–2007 when OAFlux/ISCCP data is available. All monthly mean data are linearly projected to the model grid before comparison.

Figure 2 shows that the ECDA depicts the general characteristic of the net heat flux climatology. During boreal winter, there are heat losses over the northern oceans with maxima under 250 W/m^2 along the western

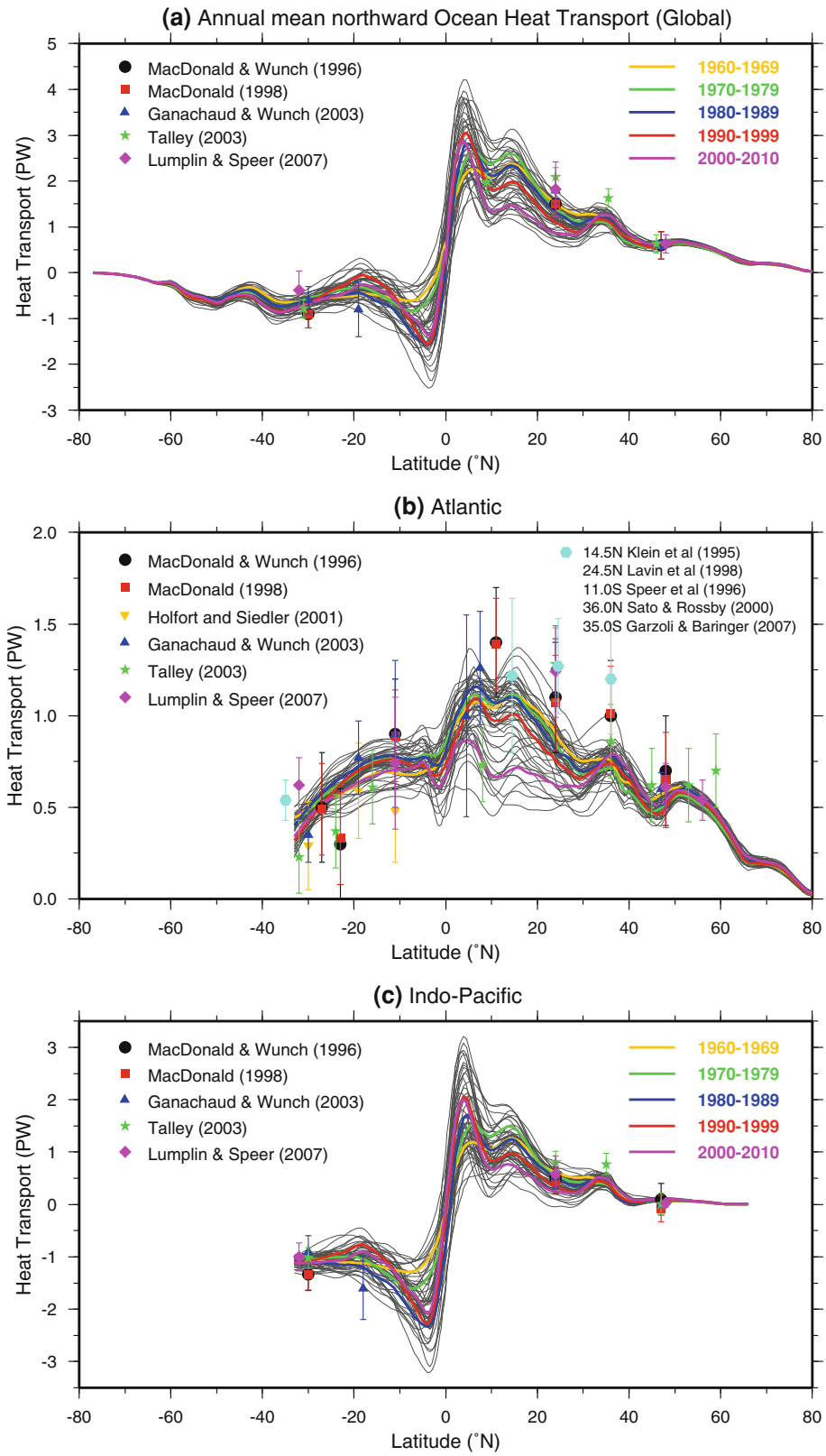

Fig. 1 Comparison of northward oceanic heat transport (unit: PW) from the ECDA (*gray lines* are annual mean for the individual 51 years (1960–2010), and *colored lines* denote 10-year mean values) with previously published estimations with *error bars* (see legend). **a**–**c** The global, Atlantic, and Indo-Pacific Oceans, respectively

boundary currents, while the tropical and southern oceans gain heat. There are hemispheric asymmetries between the summer and winter seasons, but tropical oceans still gain heat especially along the narrow equatorial upwelling areas in the Pacific and Atlantic. Compared to the OAFlux/ISCCP in Fig. 1c, the ECDA underestimates the warming

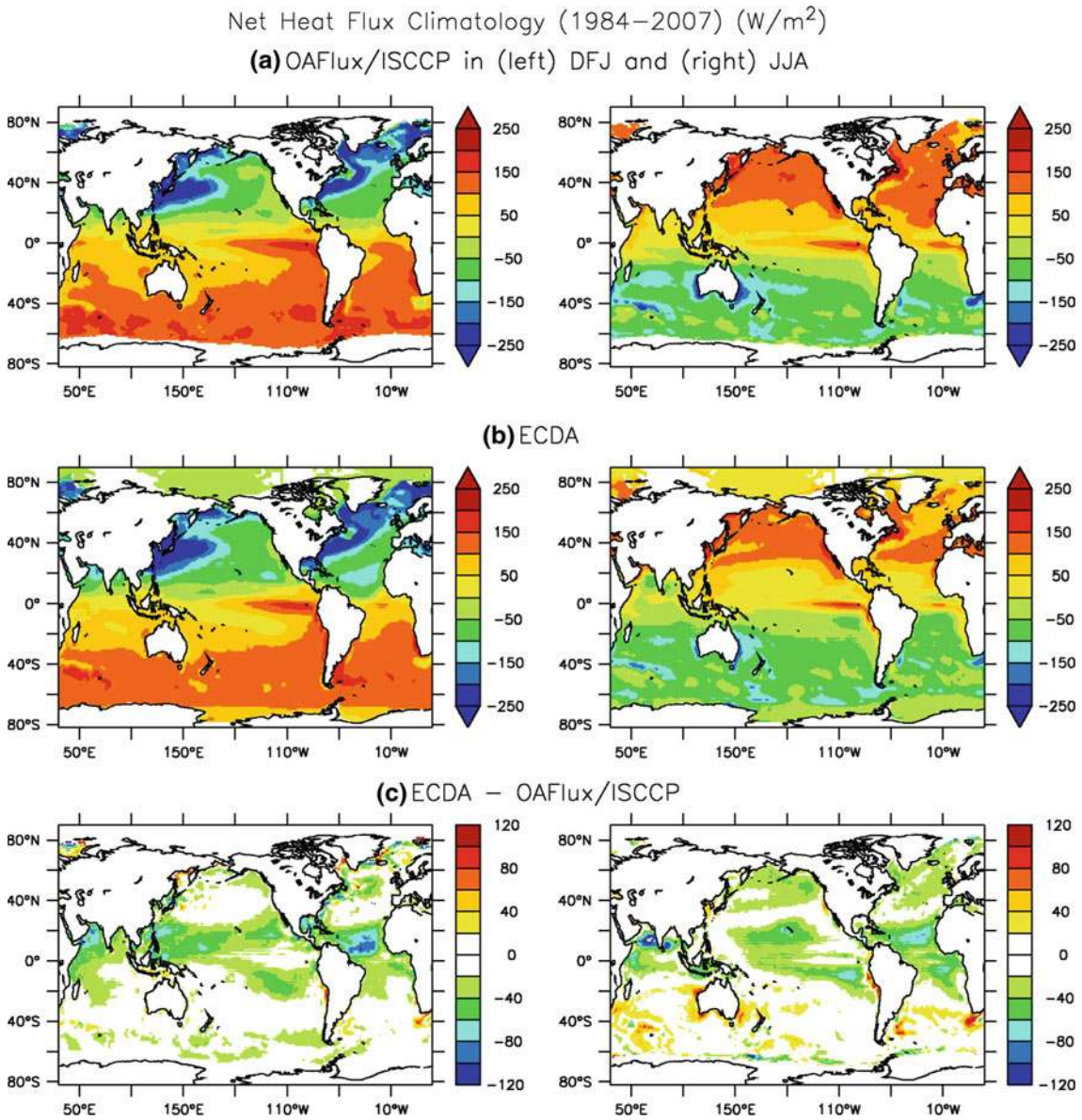

Fig. 2 Comparison of net heat flux climatology from the **a** OAFlux/ISCCP, **b** ECDA simulation, and **c** difference. *Left panels* represent boreal winter [December, January, and February (DJF)] and *rights* show boreal summer [June, July, and August (JJA)] averaged over 1984–2007

around the Tropics within 30 N(S)° throughout the year, which is consistent with the previous comparisons for the existing reanalysis (see Fig. 1 from X11). For the boreal summer, the ECDA shows cooling difference in the northern oceans and warming in the southern oceans, respectively. But the existing reanalysis (NCEP R1, NCEP R2, and CFSR) show different characteristics. NCEP R2 shows a general warming difference in the subpolar Pacific and Atlantic Oceans during the boreal summer (Fig. 1(c) from X11). The CFSR shows some significant improvements around tropics and western boundary current areas, but it still shows negative differences in the south-eastern tropical Pacific and Atlantic. It has also warm differences in the tropical Indian Ocean, western tropical Pacific, and the tropical North Atlantic (Fig. 1(d) from X11), which may be explained by any attribution of clouds and errors of shortwave radiation flux (Wang et al. 2011). Even though the atmospheric component of the ECDA is constrained by the NCEP R2, it is very hard to explain the uncertainty on the ocean net heat flux because the first guess is given by the interaction with coupled model components (atmosphere, ocean, land, and sea ice) throughout the flux exchange. It is important to emphasis that the GFDL ECDA is a fully coupled assimilation, so the fluxes are computed in the model system and not just subscribed from a given boundary condition as in an uncoupled case. Also the combined net flux from OAFlux and ISCCP itself has uncertainties.

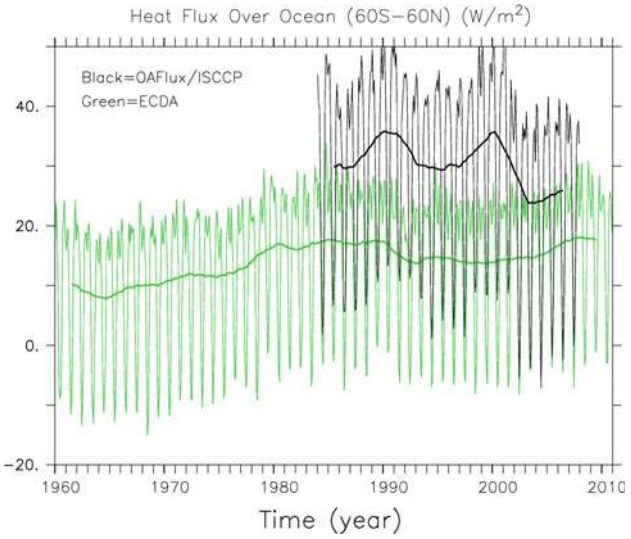

Fig. 3 Time series of the monthly mean of the net heat flux averaged over the global ocean between 60°S and 60°N from the (*black line*) OAFlux/ISCCP, and (*green line*) ECDA. *Sold thick lines* are 3-year running mean results

Figure 3 shows the mean time series of the net het flux averaged between 60°S to 60°N from the ECDA and OAFlux/ISCCP. Net heat flux estimation averaged for 1984–2007 is about 30.61 W/m^2 in OAFlux/ISCCP (black line in Fig. 3), even though it should be zero averaged in the global ocean over a long period. This imbalance is related to the overestimation of the shortwave flux in the ISCCP (Large and Yeager 2009). Net heat flux from the ECDA for 1960–2010 is about 13.97 W/m^2 (green line in Fig. 3). It steadily increases until 1985, decreases from 1985 to 2003, and increases again hereafter. No sudden jumps or strong interannual/decadal changes are found compared to the OAFlux/ISCCP, which may be associated with instrument error on the TOVS satellite, as reported by the ISCCP (http://isccp.giss.nasa.gov/projects/flux.html).

We compare the ECDA wind stress products by using two different datasets; one is ERA40 reanalysis climatology averaged for 1979–2001 (Uppala et al. 2005), and the other is QuickSCAT SOCW climatology based on scatterometer observations for 1999–2009 (Risien and Chelton

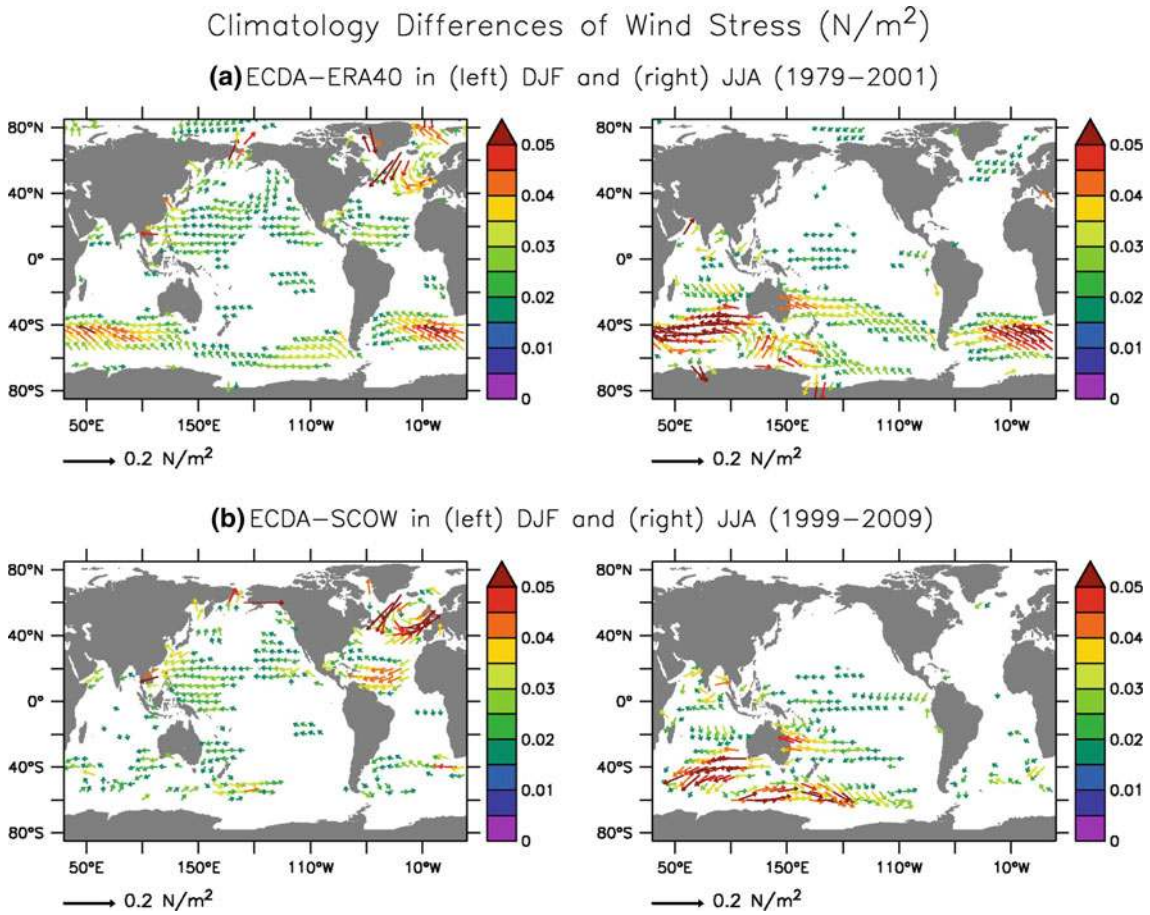

Fig. 4 Comparison of wind stress difference between the **a** ECDA and ERA40 over 1979–2001, and **b** ECDA and SCOW over 1999–2009. Difference vectors (N/m^2) are shown if their amplitudes (*shading*) exceed 0.015 N/m^2. They are also presented on every 7th (5th) point of the longitudinal (latitudinal) grid to clarify the direction. *Left panels* represent boreal winter (DJF) and *rights* show boreal summer (JJA) averaged over 1979–2001

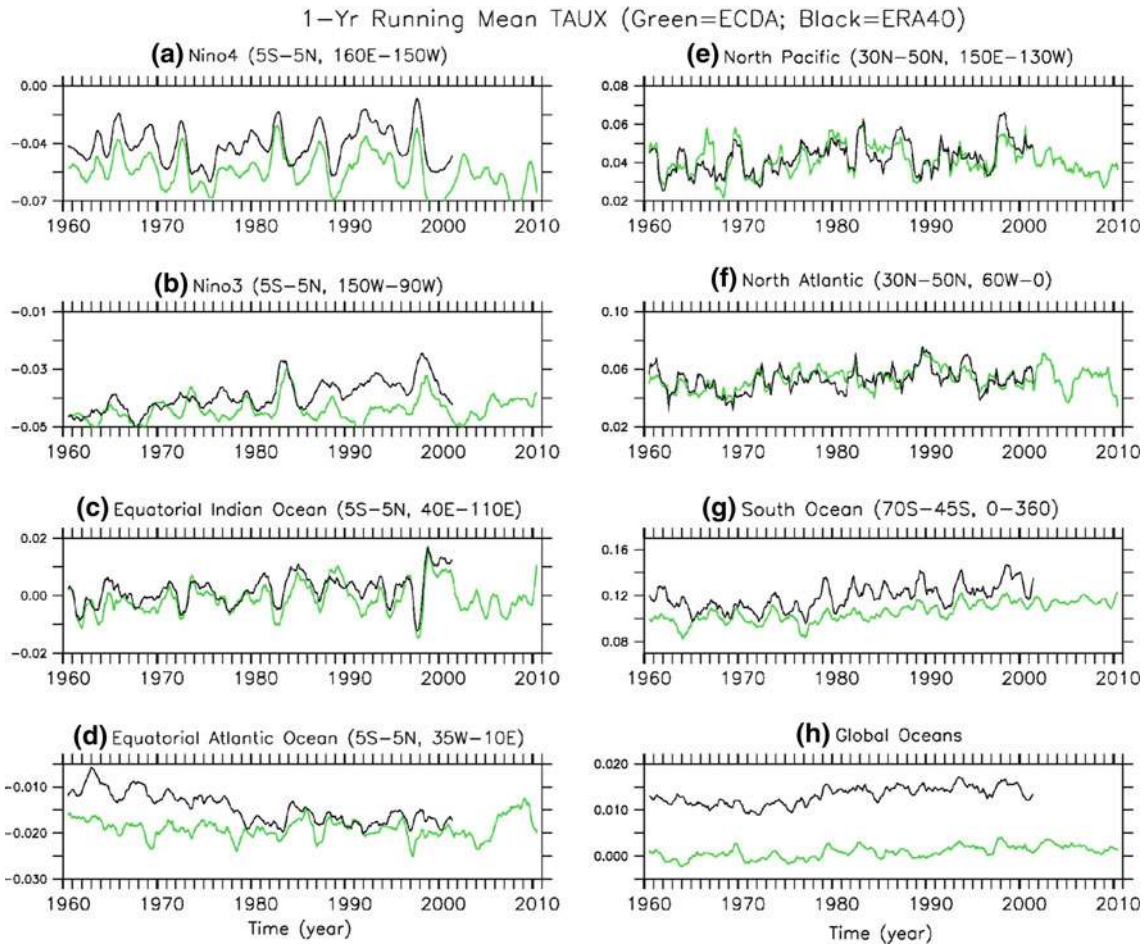

Fig. 5 Time series of 1-year running mean of zonal wind stress in several regions for (*green line*) ECDA and (*black line*) ERA40. Units are N/m^2

2008). Compared to ERA40 shown in Fig. 4a, the major differences are stronger trade wind stress in the subtropical oceans, and positive wind stress curl anomaly in the subpolar Atlantic Oceans during boreal winter. Weakening of the westerly wind stress in the high-latitude southern oceans is evident for both seasons as well. This difference is decreased when we compare with QuickScat SCOW datasets as shown in Fig. 4b, which indicates that ECDA's climatology generally agrees with the QuickScat SCOW better than ERA40. Other reanalyses (R1, R2, and CFSR) show different characteristics compared with ERA40 (see Fig. 3 from X11). Note that wind stress in R1, R2 and CFSR does not account for the effects of surface ocean currents. This may explain some of the differences in wind stress in the CFSR and ECDA. For example, the westerly wind stress in CFSR in high-latitude southern oceans is too strong relative to QuickScat SOCW (see Fig. 4 from X11). Since surface ocean currents are eastward in this area, the westerly wind stress biases will be reduced if relative velocity to ocean currents had been used in calculation of wind stress in the CFSR.

Figure 5 shows the time evolution of zonal wind stress in several regions. Since QuickScat SCOW provides only monthly mean climatology, we use only ERA40 data from 1960 to 2001 for the comparison. General interannual variability shows a good agreement in the different products, but there are some differences in the amplitude. Zonal wind is too strong in the equatorial Pacific [Nino4 (Fig. 5a) and Nino3 (Fig. 5b)] compared to ERA40, while it agrees well in the equatorial Indian (Fig. 5c) and Atlantic Oceans (Fig. 5d). At the equatorial Atlantic Ocean, easterly wind of ERA40 is relatively weak and it shows a linear trend from 1960 to 1979, which is not shown in the ECDA (Fig. 5d). As noted before, in the high latitude southern oceans (Fig. 5g), the westerly wind is weak compared to ERA40. This difference affects the mean value over the global ocean shown in Fig. 5h. The westerly winds in the high latitude southern oceans have evident upward trends as well, which is consistent with previous studies (Huang et al. 2006; Yang et al. 2007). For the CFSR (see Fig. 5 from X11), zonal wind stress agrees well with that from ERA40, but it also shows strong trade wind patterns

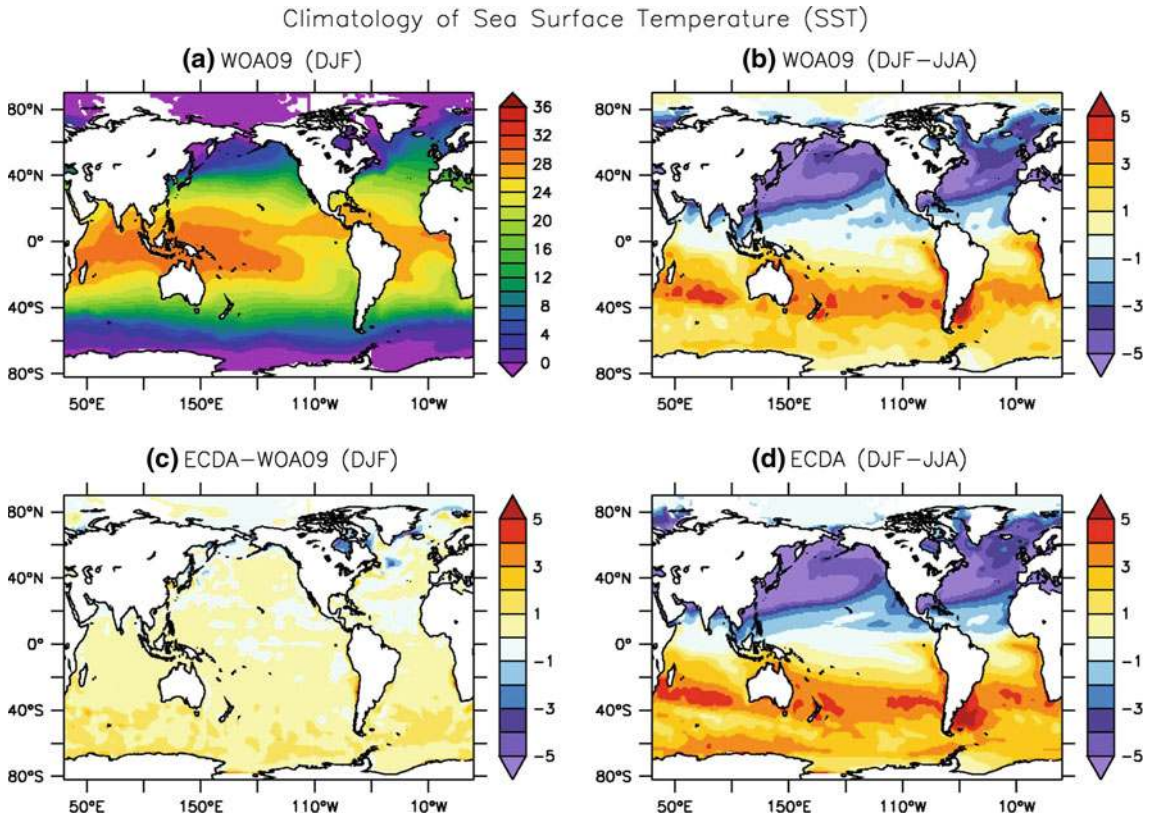

Fig. 6 Sea surface temperature (SST) from the **a** WOA09 climatology for boreal winter (DJF), and **b** seasonal difference between DJF and JJA from the WOA09 climatology. **c** SST difference between the ECDA and WOA09 climatology for boreal winter (DJF). **d** Seasonal difference between DJF and JJA from the ECDA climatology. The SST fields for the ECDA climatology are averaged for the period, 1960–2010. Units are °C

especially before 1999 in the tropical Pacific. In the equatorial Atlantic, the CFSR shows strong easterly about 0.01 N/m^2 compared to ERA40, while the ECDA shows no significant difference. Uncertainties in the reanalysis wind stress products are very difficult to qualify. The discrepancies among reanalyses may be partially caused by the differences in the definition of wind stress and systematic model biases. There is also not enough validation data over long time periods to qualify which one is better.

3.3 SST, SSS, and mixed layer depth

The climatology of SST and SSS in the ECDA is compared with that from the World Ocean Atlas 2009 (WOA09). WOA09 is a latest version of the objectively analyzed (1° by 1° grid) climatological fields of in situ temperature and salinity at standard depth levels for annual, seasonal, and monthly composite periods provided by NODC (Locarnini et al. 2010; Antonov et al. 2010). We use monthly mean data and they are linearly projected on the model grid before comparison. The climatology of SST, SSS and their seasonal variations in the ECDA agree well with those of WOA09. However, the ECDA shows a warm bias especially in the southern oceans, which is associated with the systematic bias from the base model, CM2.1 (Fig. 6c). The ECDA SSS is also a little high near the Amazon River discharge area, Gulf of Guinea, Bay of Bengal, and the coastal area along the Gulf Stream, which is attributable to the uncertainty of river runoff and precipitation (Fig. 7c). Note that the seasonal change in SSS is very well simulated by the ECDA (compare Fig. 7b and Fig. 7d), while seasonal change is absent in the CFSR due to a too strong nudging to the annual mean SSS climatology (see Fig. 6(e) from X11).

In Fig. 8, the climatology of mixed layer depth (MLD) is compared with objective analyzed product based on individual temperature and salinity profiles up to September 2008. This product can be obtained from http://www.lodyc.jussieu.fr/∼cdblod/mld.html (de Boyer Montégut et al. 2004). We use the MLD definition defined by fixed density criterion; depth where density increase compared to density at 10 m depth equals 0.03 kg/m^3. The general features of MLD climatology described by observations are well simulated, but there are some differences in the ECDA. In the boreal winter shown in Fig. 8e, the ECDA overestimates the MLD around the northwestern Pacific and Atlantic Oceans following the subtropical gyre system.

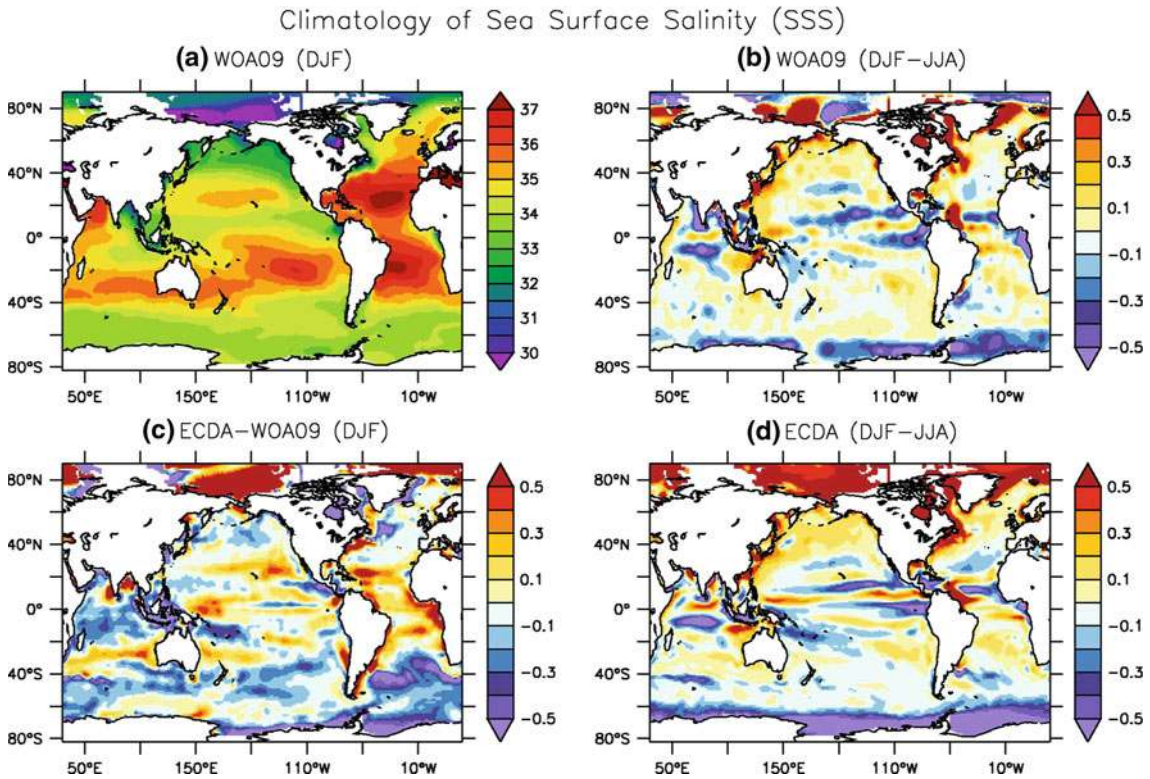

Fig. 7 The same as Fig. 6 except for the sea surface salinity (SSS). Units are psu

Large differences around the subpolar North Atlantic areas are also found, which may be related to the uncertainties in surface fluxes and deficiencies in model physics on deep convection areas in the winter season. This is also related to the large departure around the high-latitude southern oceans in boreal summer (Fig. 8f).

3.4 Upper ocean heat content and SSH

The upper ocean heat content (HC) is one of the key indicators of climate variability from seasonal to long-term time scales, and an accurate ocean initialization of HC in coupled climate models could be an important factor in enhancing skill in decadal climate predictions (Smith et al. 2007; Meehl et al. 2009). Estimation of HC using data assimilation systems can be also affected by many factors including uncertainties in model bias, assimilation method, surface forcing, and changes in the input data (Carton and Santorelli 2008). In this section, we estimate the HC by averaging the temperature field in the upper 300 m (HC300) following the companion paper (X11). For comparison, we use gridded yearly temperature anomalies at 16 standard depth levels from 1955 to 2010 provided by NODC (Levitus et al. 2009). We also use AVISO (Archiving, Validation and Interpretation of Satellite Oceanographic data) altimetry datasets that merge the TOPEX/Poseidon, Jason-1, ERS-1/2, and Envisat satellite measurements on 1/3° by 1/3° grid points and are weekly updated since 1993 (Ssalto/Duacs User HandBook 2008). NODC (AVISO) data used in this section are averaged into yearly (monthly) mean and linearly interpolated to match the ECDA grid.

The linear trend of HC300 in 1993–2008 shows very similar patterns between the NODC (Fig. 9a) and ECDA (Fig. 9b). Significant increasing trend patterns in the western Pacific and the subpolar North Atlantic are resolved well by the ECDA. They are clearly related to the ENSO phenomena and the weakening of the North Atlantic subpolar gyre system during this period (Hakkinen and Rhines 2004). For the North Pacific, the ECDA simulates an increasing HC in the central North Pacific, and a decreasing HC south of Alaska including off the west coast of North America, which is similar to the PDO pattern (Mantua et al. 1997). The ECDA agrees with NODC even around the tropical Atlantic and the Indian Ocean where the CFSR shows low performance (see Fig. 8(b, e) from X11). The ECDA shows relatively strong linear trend around the Gulf of Mexico including Caribbean Sea and some area of the southern Atlantic Oceans, while negative trends are found around the high-latitude southern oceans.

The linear trend of SSH from the ECDA (Fig. 9d) is generally consistent with that of HC300. Negative trend is found around equatorial eastern Pacific, high-latitude southern ocean and the south of Alaska including off the

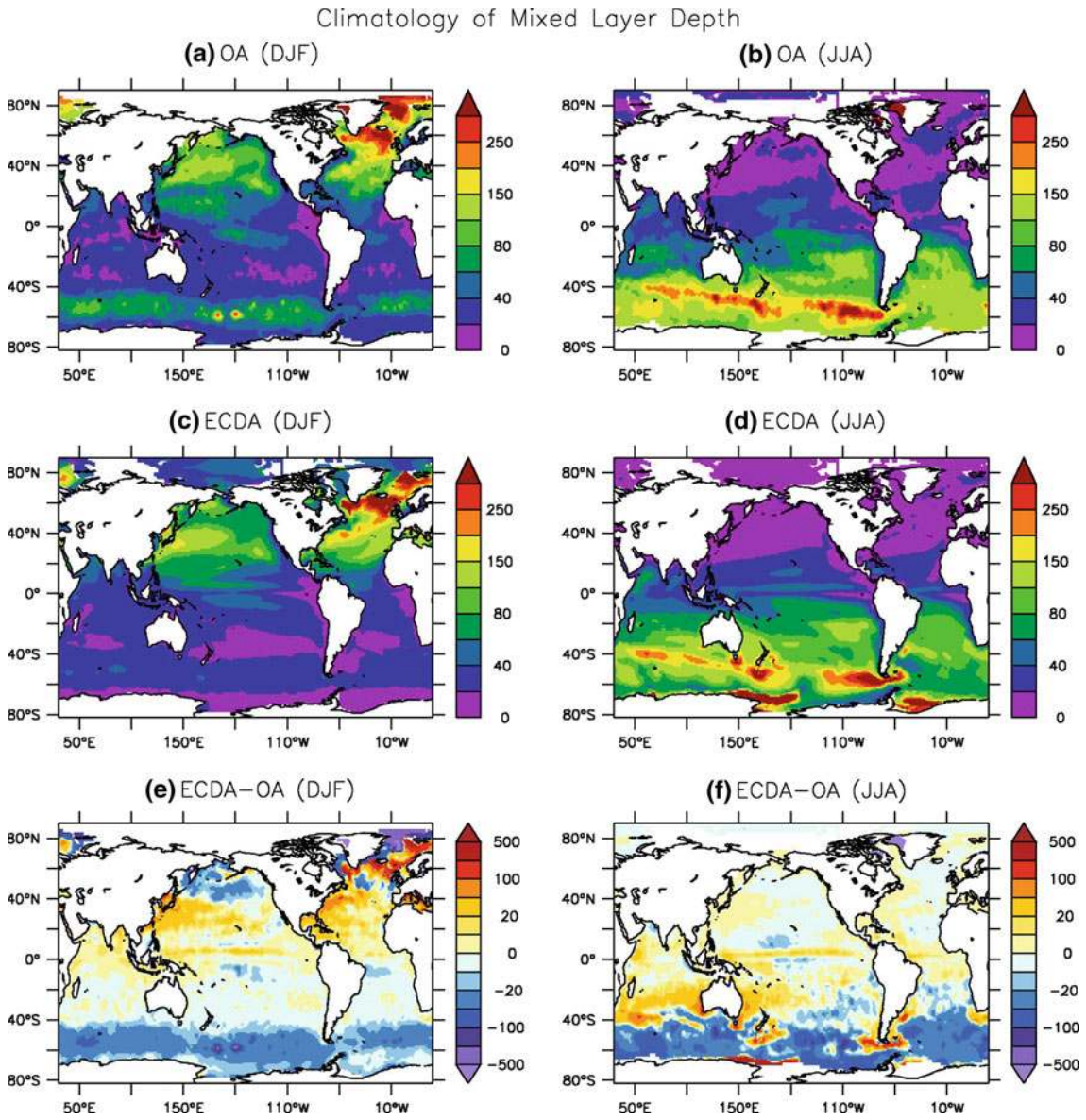

Fig. 8 The climatology of the mixed layer depth (MLD) for (*left panels*) boreal winter (DJF) and (*right panels*) boreal summer (JJA). **a**, **b** Objective analysis from de Boyer Montégut et al. (2004), **c**, **d** ECDA climatology averaged for 1960–2010, and **e**, **f** difference between the ECDA and observations. Units are m

west coast of North America. However, the positive tendency in the observed AVISO altimetry is more prominent around most of the oceans especially for the southern area including the Indian Ocean (Fig. 9c). Previous studies investigated the recent sea level change from the analyses of independent observations in order to assert the sea level balance among them (total sea level change from satellite altimetry can be explained as the sum of the steric height contribution obtained by Argo profiles and any variability in ocean mass observed from GRACE satellite). However, sea level trend does not agree within the error bounds of each observing system especially over the South Indian Ocean (Willis et al. 2008; Chang et al. 2010; Leuliette and Willis 2011). Most disagreements in Fig. 9 are found around the southern oceans including the Indian Ocean, so it may be related to this sea level discrepancy issue.

The correlations of SSH between the ECDA and the AVISO altimetry also show very little agreement around the southern oceans (Fig. 10). There are high correlations only around the tropical and subtropical Pacific, eastern North Pacific, subpolar North Atlantic (Fig. 10a). The ECDA also shows reasonable correlation patterns around the equatorial Atlantic where the CFSR shows low correlation with altimetry (see Fig. 10(a) from X11). The RMSD of SSH between the ECDA and altimetry is generally large near the western boundary currents, and in mid- and

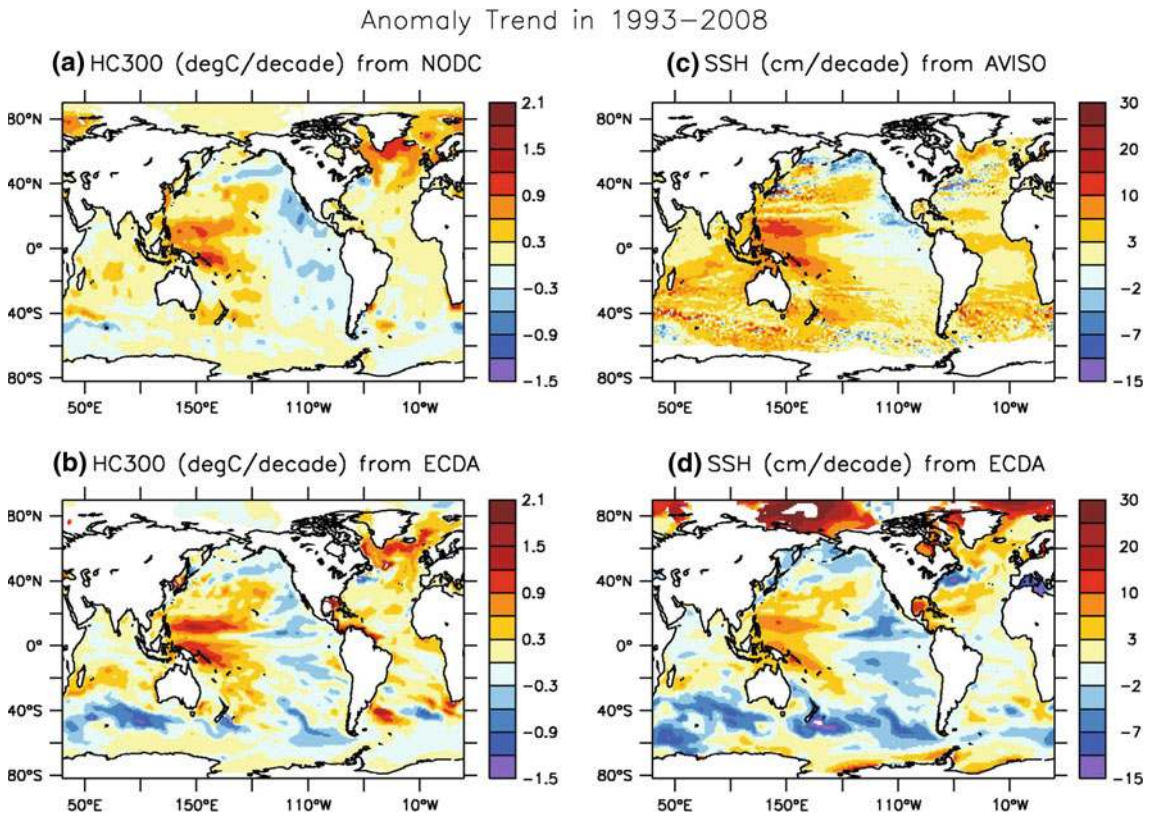

Fig. 9 Linear trend for 1993–2008 in the upper 300 m heat content (HC300, °C/decade) anomaly from the **a** NODC and **b** ECDA, and in the sea surface height (SSH, cm/decade) anomaly from the **c** AVISO and **d** ECDA

high-latitude southern oceans (Fig. 10b). We also provide same statistics during Argo period for 2004–2010 (Fig. 10c, d). Results show that correlation and RMSD are improved around the subtropical Pacific, equatorial Atlantic, Indian Ocean, and southern oceans during Argo period (Fig. 10e, f). This result indicates that the assimilation of Argo T–S profiles is also correcting SSH fields by changing density fields in the ECDA system. Note that Altimetry information is not used for our ECDA system and RMSD is large around the western boundary and high-latitude southern ocean where a meso-scale oceanic phenomenon is active. Therefore, we can expect an additional improvement of SSH as well as HC300 fields when altimetry data is directly assimilated to the ECDA system based on a high resolution model resolving the meso-scale oceanic eddies in the near future.

In order to investigate the variability of HC300 in detail, we estimate the HC300 anomaly over the selected regions from 1960 to 2010 (Fig. 11). For the validation, we use three different objective analyzed products based on in situ temperature profiles (NODC2005 Levitus et al. 2005, NODC2009 Levitus et al. 2009, and EN3 Ingleby and Huddleston 2007) and estimate their difference ranges as the gray lines in Fig. 11. The width of the gray line represents the uncertainties arising from the choice of objective mapping methodology, the method of data quality control such XBT correction and Argo pressure sensor errors, and the effects of irregular and sparse sampling among three different data sources. Since NODC2005 provides gridded temperature data up to 2003, anomalous HC300 is derived by removing the 1960–2003 climatology for each data set separately. Strictly speaking, this comparison is not completely independent because same observed profiles are being used in the ECDA, NODC2005, NODC2009, and EN3. However, as we previously mentioned, three datasets (NODC2005, NODC2009, and EN3) also show significant differences even though they used same in situ temperature profiles. Estimation of HC300 using data assimilation systems can be affected by not only input data, but also many other factors including uncertainties in model bias, assimilation method and surface forcing. Therefore, it would be meaningful to compare the ECDA to existing objective analyzed datasets because they use different frameworks to generate gridded HC300 fields. In addition, it is very hard to find out independent in situ profiles since the ECDA used them as many as possible to complete reanalysis.

The phase of the variability of HC300 matches very well for the whole analyzed period 1960–2010. The amplitude of the HC300 also agrees well with observations except for

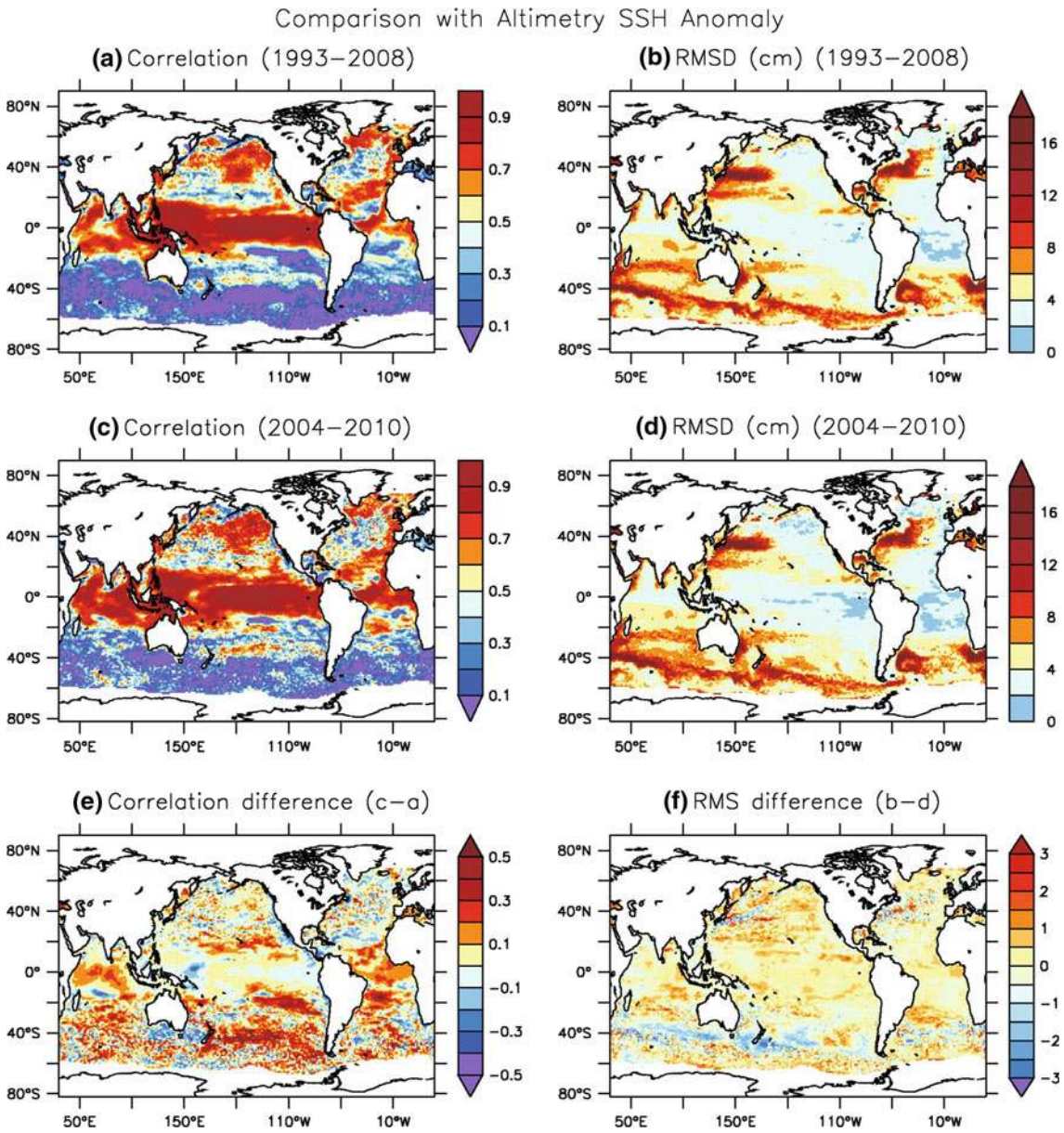

Fig. 10 **a** Anomaly correlation and **b** Root Mean Square Difference (RMSD) of SSH between the ECDA and AVISO altimetry for 1993–2008. **c**, **d** represents correlation and RMSD for 2004–2010. **e**, **f** are their differences

several discrepancies as follows; For the first decade around 1960–1970, warm differences are found in the tropical western Pacific (Fig. 11a), equatorial Atlantic (Fig. 11c), central North Pacific (Fig. 11d), and North Atlantic (Fig. 11g), which may be related to the spin up period of the ECDA system. During 1970–2000, the North Atlantic (Fig. 11g) and Pacific (Fig. 11d) show slight cold anomalies compared to observations. In the twenty-first century simulation, there are several warm differences again around equatorial eastern Pacific (Fig. 11b), equatorial Atlantic (Fig. 11c), subtropical northeastern Pacific (Fig. 11e), subtropical southeastern Pacific (Fig. 11f), North Atlantic (Fig. 11g), and subtropical North Atlantic (Fig. 11h). These consecutive differences (warm, cold and warm differences in time) generate relatively strong decadal change of the HC300 for the global ocean (Fig. 11i), even though the difference is not large compared to the uncertainties among observations. Levitus et al. (2009) showed that correcting for XBT biases reduces the magnitude of the inter-decadal variability of previous estimates of heat content, so we may expect additional improvement when we applied to new XBT correction methods in the near future when the XBT community publishes an official method. As for the comparison with CSFR in the previous study, large discrepancies between CFSR and NODC are found especially for the equatorial Atlantic (see Fig. 9(c) from X11), while the ECDA

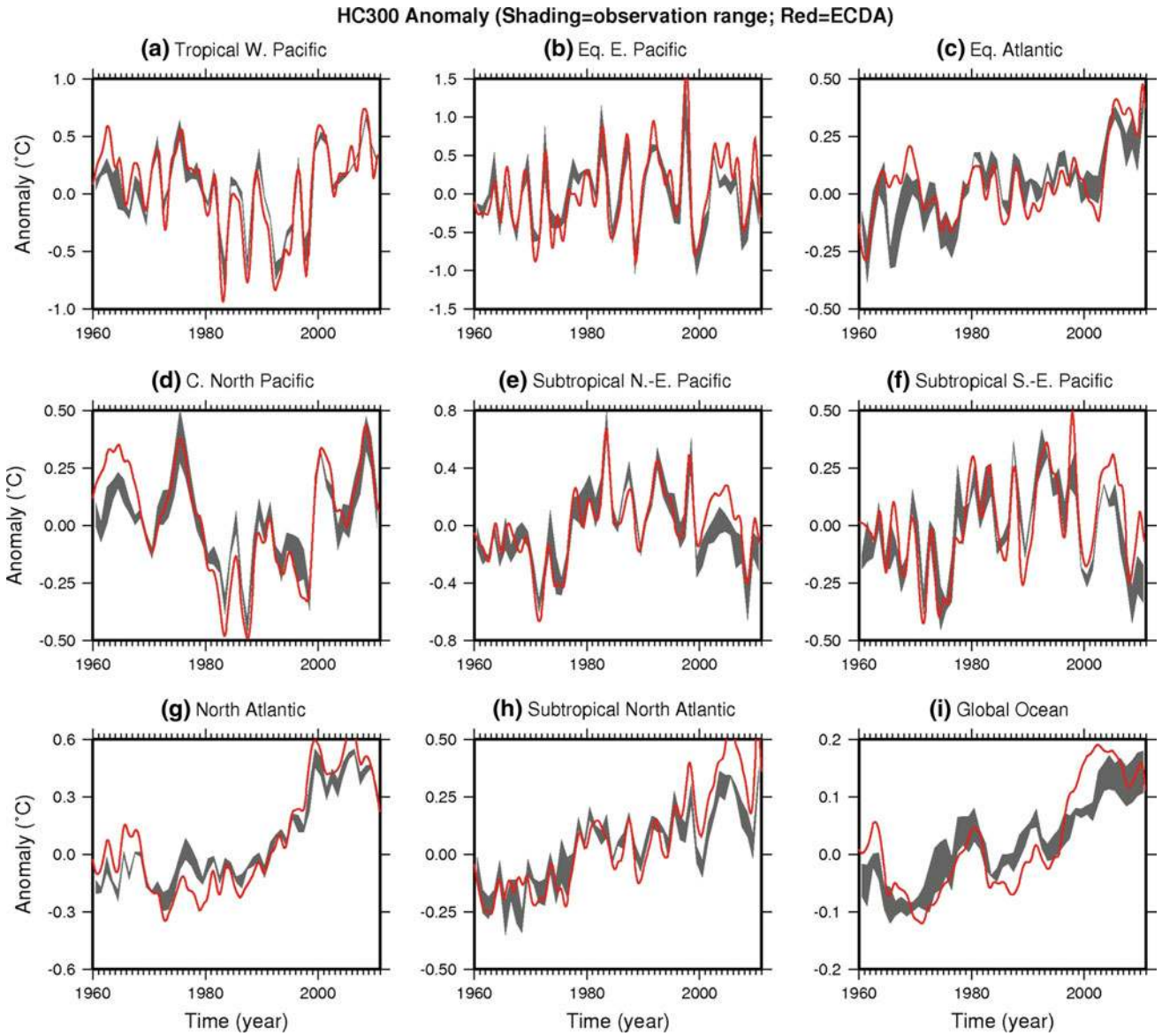

Fig. 11 Time series of 1-year running mean of HC300 anomaly averaged in various boxes for the (*red line*) ECDA. *Shading line* indicates the different range among the NODC2009, NODC2005, and EN3 objectively analysis datasets based on only in situ data. Reference period for the anomaly is 1960–2003. **a** Tropical western Pacific (130°E–190°E, 20°S–20°N), **b** equatorial eastern Pacific (210°E–270°E, 5°S–5°N), **c** equatorial Atlantic (310°E–10°E, 10°S–10°N), **d** central North Pacific (180°E–220°E, 20°N–40°N), **e** subtropical northeast Pacific (220°N–270°N, 5°–25°N), **f** subtropical southeast Pacific (220°N–280°N, 5°S–25°N), **g** subpolar North Atlantic (280°E–350°E, 30°N–60°N), **h** subtropical North Atlantic (280°E–360°E, 5°N–25°N), and **i** Global Ocean (0°–360°E, 70°S–70°N)

from this study shows a reasonable variability except around 1965–1970 (Fig. 11c).

3.5 Equatorial oceans

Since TAO (Tropical Atmosphere Ocean) mooring data provide subsurface temperature and independent current information at a fixed location for enough time periods, and the tropical ocean is very important for the long-lead seasonal forecast, it is worth investing the performance of the ECDA system around the equatorial areas in detail.

Figure 12 shows the departures of the ECDA temperature from the TAO temperature as a function of depth and time at four sites of the TAO array. Vertical structure of the correlation and RMSD (Root Mean Square error Difference) between the ECDA and TAO are also presented together. Temperature departures are mostly negative at depth below 200 m and slight positive (negative) near the surface in the upper 100 m especially for the western (eastern) Pacific. The correlation decreases below 200 m depth, which is related to the significant cold biases on most TAO sites. The vertical average of correlation

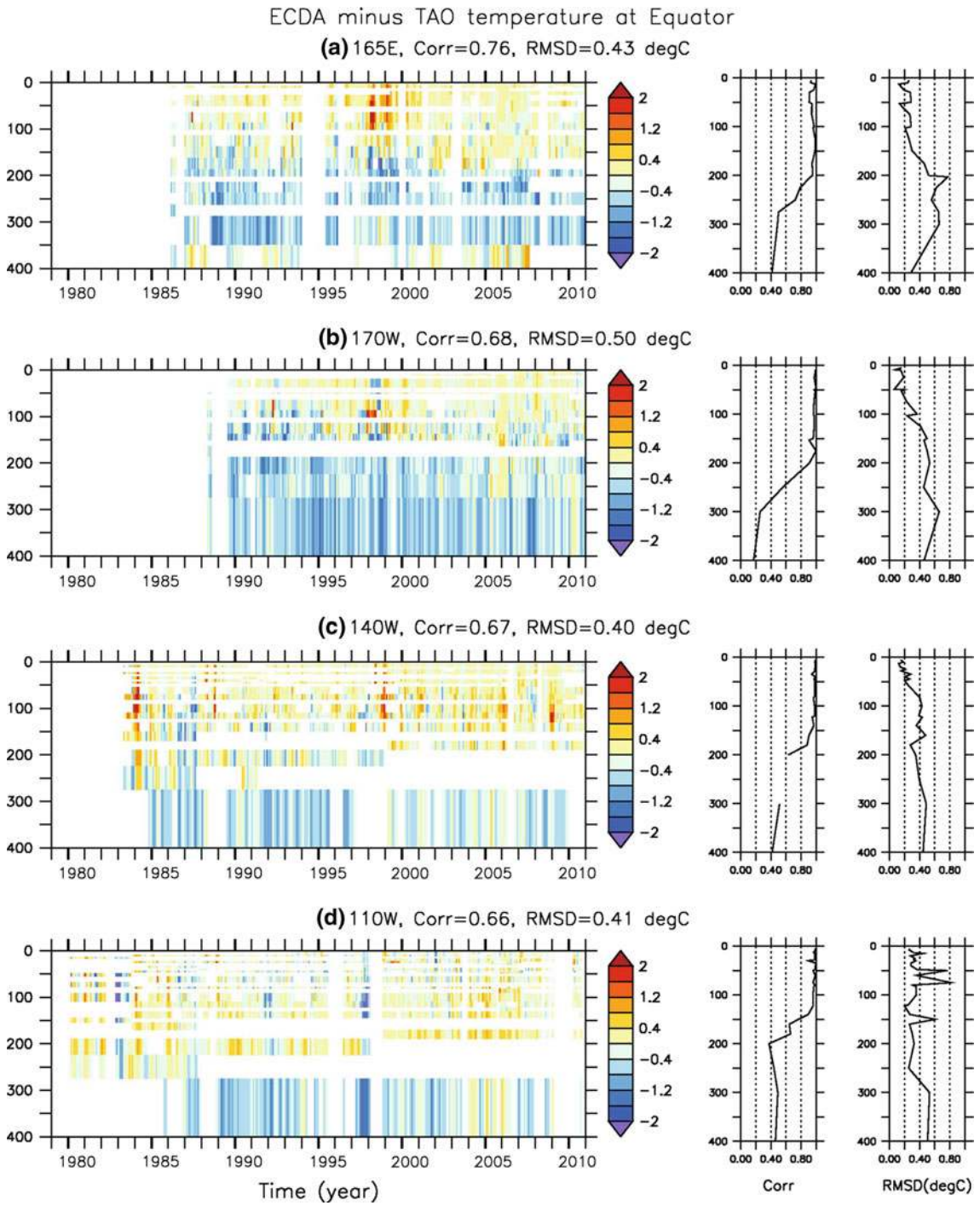

Fig. 12 Difference between the ECDA and TAO temperature (°C) at four equatorial TAO mooring sites at **a** 165°E, **b** 170°W, **c** 140°W, and **d** 110°W. *Right two panels* show the vertical structure of the correlation coefficient and Root Mean Square Difference (RMSD) between the ECDA and TAO averaged for the analyzed periods

coefficients are larger than 0.6 and RMSD is less than 0.5 °C. The CFSR shows better correlation, but larger RMSD than those of the ECDA (see Fig. 11 from X11).

For the zonal velocity analysis at the equator of the Pacific Ocean, the ECDA reveals that overall negative anomalous current compared to TAO observations (Fig. 13). This indicates that the ECDA simulates strong South Equatorial Current (SEC) and weak Equatorial Under Current (EUC), which may be related to a possible high background mixing used in the ocean model. There found no significant vertical change for the correlation and RMSD. The vertical average of correlation coefficients is

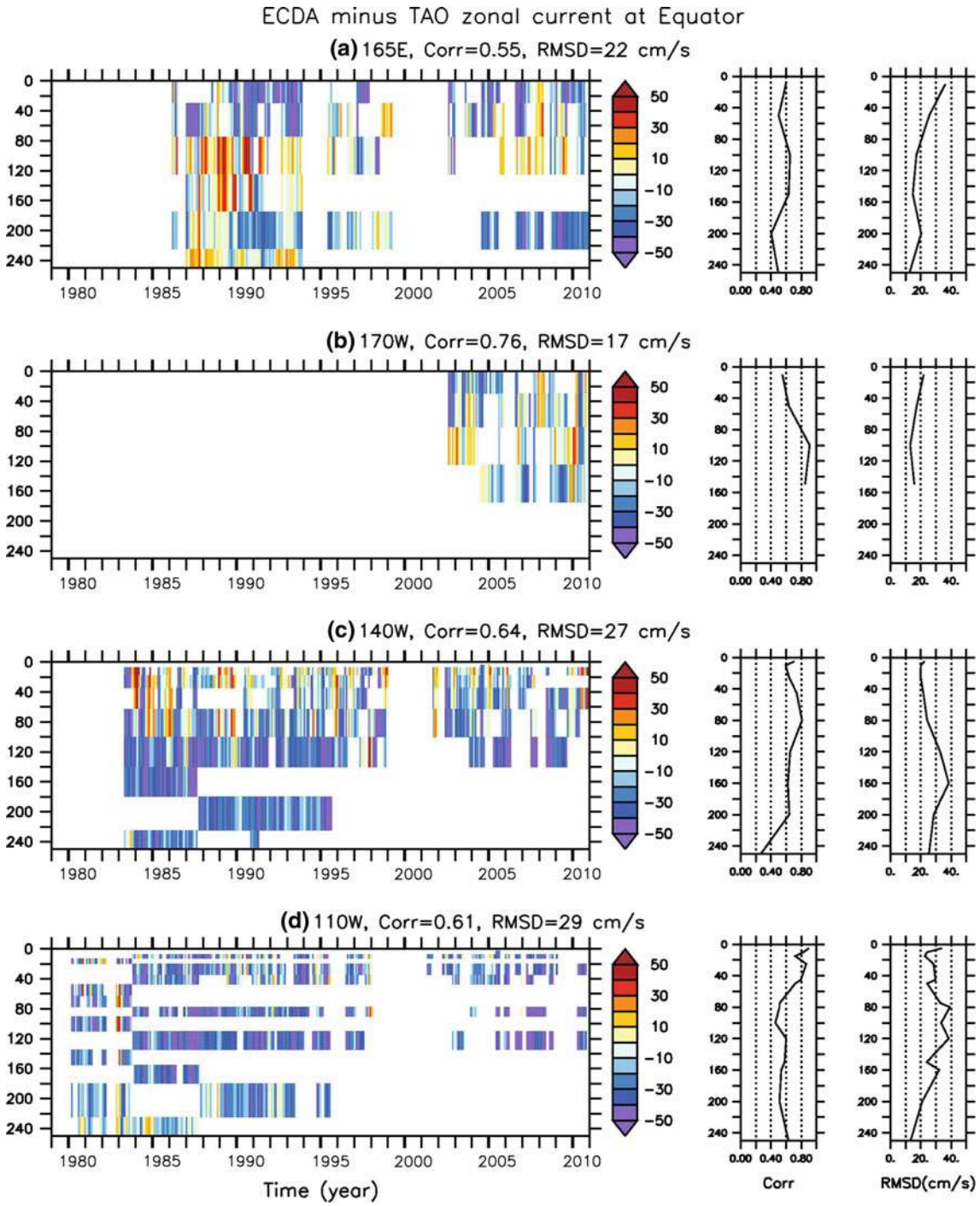

Fig. 13 The same as Fig. 12 except for the zonal current (cm/s)

larger than 0.5 and RMSD is less than 30 cm/s, which are comparable with those of CFSR (see Fig. 12 from X11).

Strong SEC is consistent with the strong trade wind stress near the equatorial Pacific as shown in Fig. 5a, b. This overestimated SEC driven by the stronger trade winds causes warm water to pile up in the western Pacific, so the surface temperature is increased (decreased) in the western (eastern) Pacific shown in Fig. 12. However, the assimilation of the observed temperature and salinity profiles helps correct the anomalous thermocline slop interacting with coupled model dynamics every time step, so we cannot understand all mechanisms causing the systematic biases shown in the ECDA system. For example, it cannot be explained by an equatorial dynamics why the ECDA underestimates the EUC together with strong wind stress and subsurface cold biases below 200 m depth, given that

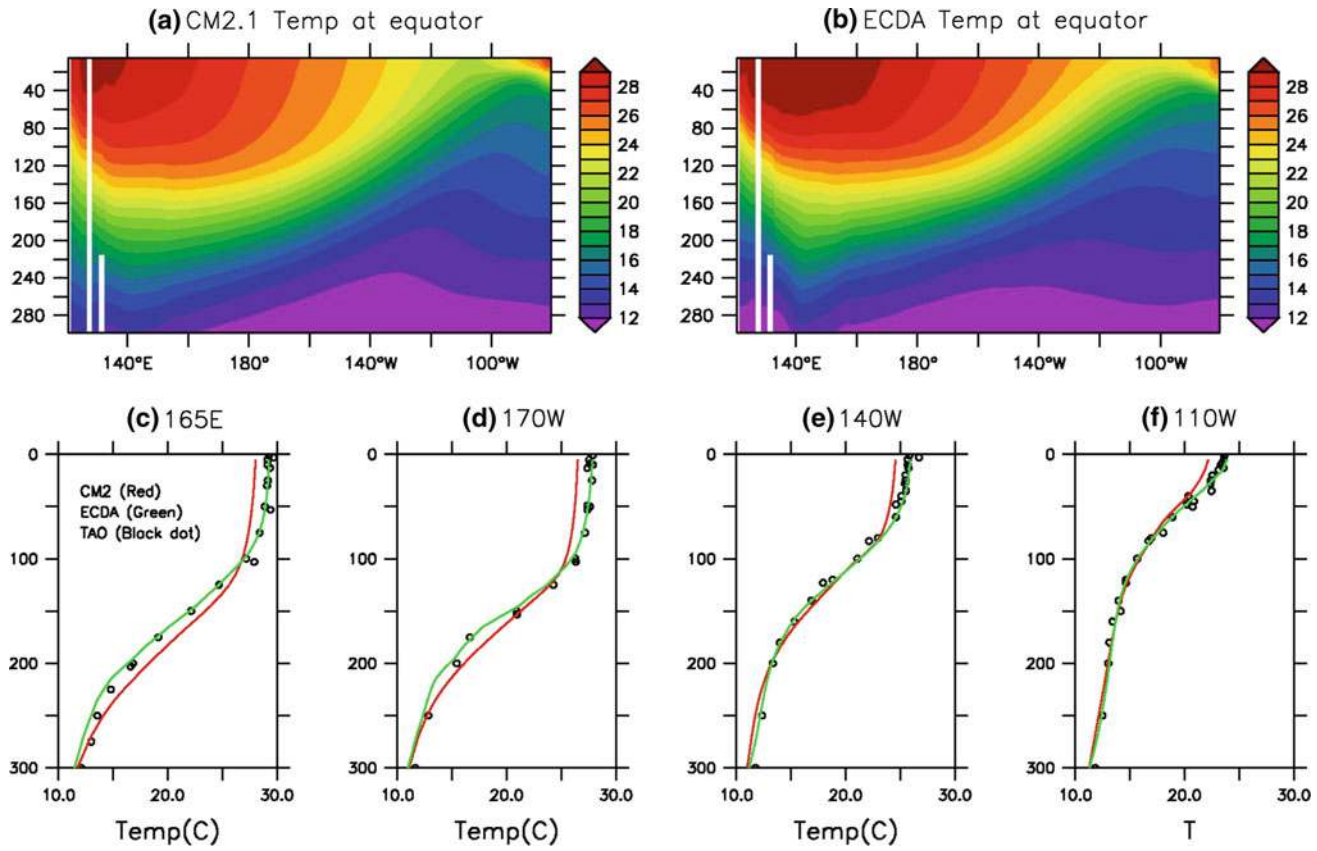

Fig. 14 Mean temperature at the equator from **a** CM2.1 and **b** ECDA. **c–f** Mean vertical profiles at the four longitudes marked from (*red line*) CM2.1, (*green line*) ECDA, and (*black dot*) TAO observations

the EUC is the eastward subsurface return flow only to rectify the water mass imbalance between the east–west pressure gradient.

In order to identify possible sources of systematic bias in EUC, we investigated bias pattern of the ECDA base model, CM2.1 from the IPCC historical simulations. For the historical simulations, the 10 ensemble members using CM2.1 were integrated using temporally varying anthropogenic and natural aerosol records from 1861 to 2020. For the comparison, we conducted a set of 10-member ensemble for 1960–2010. Figures 14 and 15 show the subsurface structures of the mean temperature and zonal current at the equator. Compared to TAO observations, a surface cold bias of CM2.1 is evident in all TAO sites, along with a warm bias around the thermocline especially in the western Pacific (red lines in Fig. 14). Meanwhile, CM2.1 simulates mean EUC well (red lines in Fig. 15), which is the consistent with the previous study (Wittenberg et al. 2006). The ECDA effectively corrects biased temperature fields (green lines in Fig. 14), but the magnitude of zonal current is also changed (green line in Fig. 15). This result shows that the assimilation of T–S only without subsurface current observations is likely to degrade the magnitude of reanalyzed current, even though it was correctly simulated under pre-determined optimized mixing coefficients. Here, note that the variability of current is significantly improved in the ECDA compared to that of CM2.1 [The vertical average of correlation coefficients between CM2.1 and TAO is less than 0.2 (not shown)], so we cannot generalize that the current reanalysis is degraded in the ECDA system. In Fig. 10, we showed that the assimilation of Argo T–S profiles is improving SSH fields due to proper density correction. Meanwhile, this result shows that the T–S assimilation cannot always guarantee an improvement of other variables because climate models contain many error sources in the values of model parameters, which is also related to the recent study on parameter correction with coupled data assimilation (Zhang et al. 2012). EUC bias could be also associated with the salinity bias since salinity affects the density fields. However, salinity bias is significantly decreased since 1993 due to pseudo and Argo salinity profiles (see Fig. 18 with corresponding description at the next section). Meanwhile, EUC bias lasts even after Argo period. Therefore, we cannot determine that the EUC bias is related to salinity bias in the ECDA system. As we mentioned before, it is not easy to explain physical mechanisms on systematic errors of the ECDA. In addition, the purpose of this study is not to

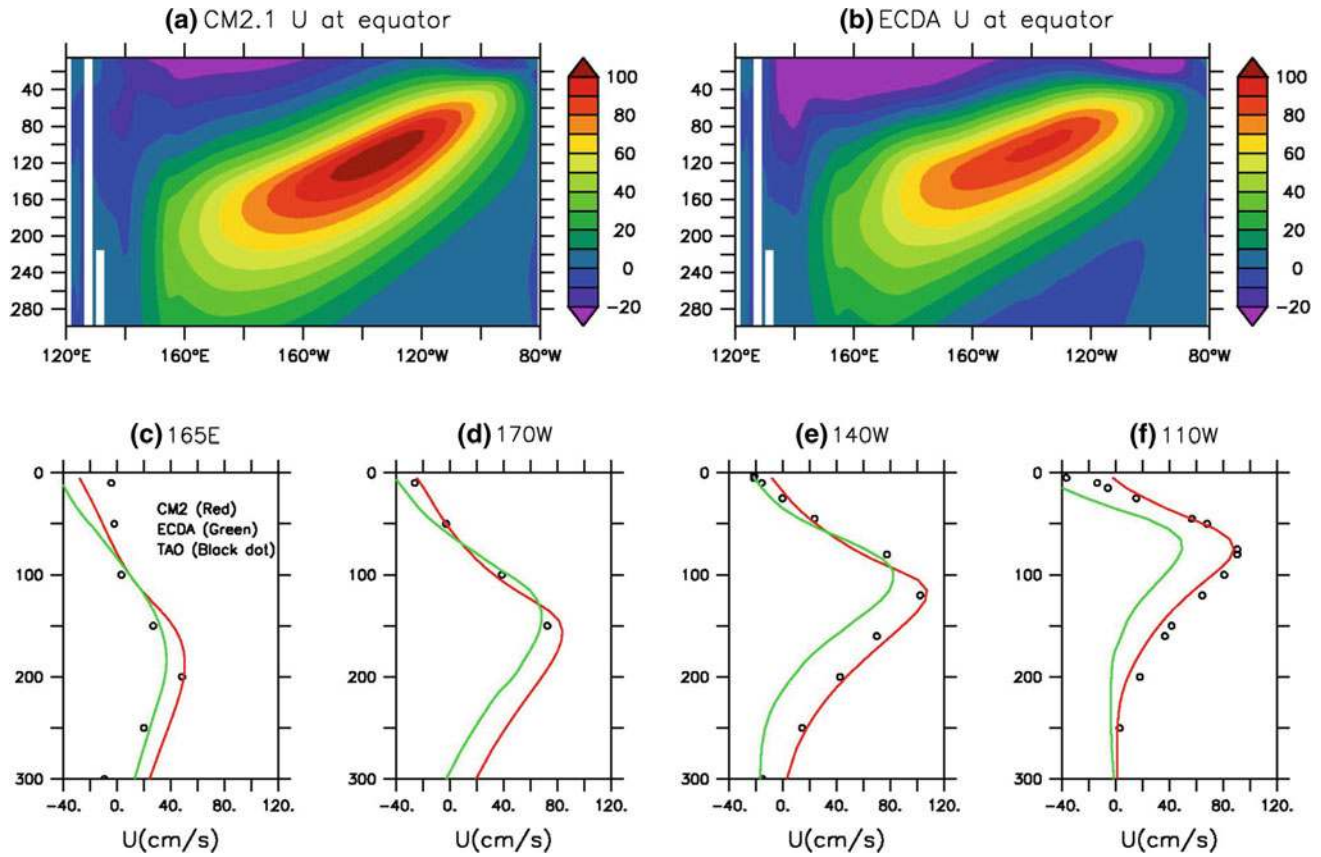

Fig. 15 The same as Fig. 14 except for the zonal current

analyze detailed variability of the equatorial oceans, but provide the general assessment of the new reanalysis from the global coupled data assimilation system. We expect that more detailed analyses will be carried out in separate studies focusing on systematic errors and their physical relationship in assimilation models.

Using another independent datasets, OSCAR (Ocean Surface Current Analysis-Real Time) measuring the mean currents in the top 30 m (Bonjean and Lagerloef 2002), we validate the surface zonal current of the ECDA. The ECDA has a stronger westward current (RMSD = 18 cm/s) during 1993–2010 when OSCAR data is available (Fig. 16a), which is consistent with our previous comparison with TAO data. Meanwhile, anomalous time series of the zonal current shows that the ECDA simulates the variability of the zonal current very well, except the ECDA underestimates the eastward current during the strong El Nino event, 1997 (Fig. 16b). The anomalous correlation between ECDA and OSCAR is 0.79, as compared to the CFSR (correlation is 0.61 and RMSD is 31 cm/s with significant pattern change in 1999, see Fig. 13 from X11). Around very narrow equatorial band (160°E–120°W and 2°S–2°N in Fig. 16), the ECDA underestimates the eastward surface current during 1997 El Nino, but we cannot generalize that the ECDA cannot resolve the strong El Nino pattern. Figure 17 shows the same time series with Fig. 16 but for Nino 3 region (150°W–90°W and 5°S–5°N). In this area, the ECDA simulates well eastward current during the 1997 strong El Nino event. The anomalous correlation between ECDA and OSCAR is also calculated much higher as 0.90.

In order to confirm the general climatology of the equatorial temperature, salinity and any possible drift found in the CFSR, we investigate temperature and salinity difference fields for selected analysis periods. For comparison, we use EN3 data instead of NODC because EN3 is based on in situ data and has a monthly resolution for both temperature and salinity up to 2010. NODC also provides gridded temperature and salinity fields, but their salinity fields are only 5-year mean values up to 1998 (Boyer et al. 2005). It is important to emphasize that it does not mean that EN3 or NODC is viewed as the truth, but gives us a common analysis to show differences.

In the climatology of the EN3 temperature fields, the thermocline slopes upward from west to east in the equatorial Pacific and Atlantic, while in the Indian Ocean slopes downward from west to east (Fig. 18a). A surface cold bias is evident in CM2.1. Warm biases along the thermocline are seen in the equatorial western Pacific and the Atlantic Ocean. Another cold biases exhibit below thermocline in

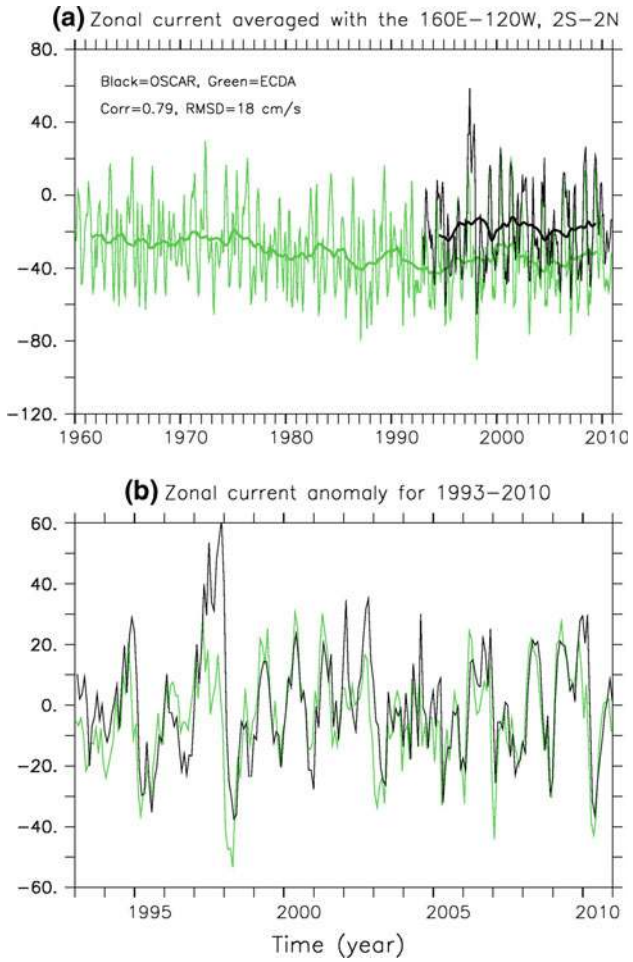

Fig. 16 Comparison of zonal current averaged within the *box*, 160°E–120°W, 2°S–2°N from the (*black line*) OSCAR and (*green line*) ECDA. *Sold thick lines* indicate 3-year running mean results. Unit is cm/s. **b** Zonal current anomaly from the (*black line*) OSCAR and (*green line*) ECDA in which their respective means for 1993–2010 are removed

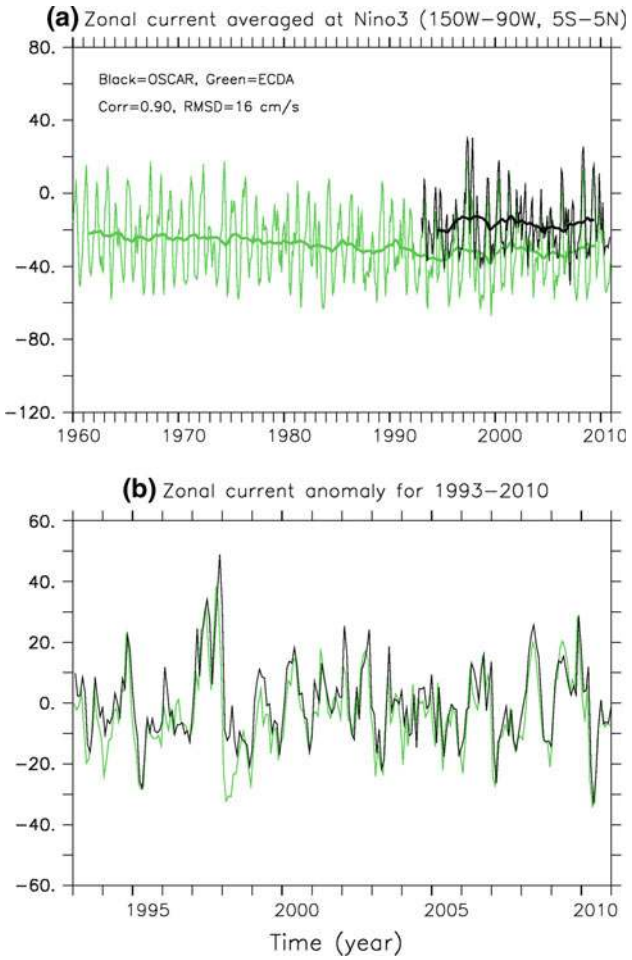

Fig. 17 The same as Fig. 16 except for Nino 3 region (150°W–90°W, 5°S–5°N)

the Pacific and Atlantic Oceans. In the Indian Ocean, there found substantial warm bias below thermocline (Fig. 18b). The ECDA temperature still has a common cold bias more than 0.5 °C near the thermocline and it exists up to 500 m in the central Pacific during 1960–1992 (Fig. 18b). In the central Pacific, this negative difference decreases in time and turns to positive less than 0.5 °C near the central-eastern Pacific around 100–200 m depth during 2003–2010 (Fig. 18d). For the western Pacific, there is systematic warm bias more than 1 °C near the surface that is related to the consistent strong wind stress as we previously discussed. At the subsurface oceans along the western boundary coastal area, there are systematic cold and warm biases to the 160°E (200°W). These systematic biases are consistent even during the Argo period after 2003. Subsurface warm biases exceeding 0.5 °C are also evident in the equatorial western Atlantic around 150 m and below 500 m depth. However, these warm biases decrease in time due to the assimilation of Argo profiles.

For the salinity climatology, the equatorial Atlantic is much saltier than the other two ocean basins in the top 300 m (Fig. 19f) in which CM2.1 experiences freshening bias (Fig. 18g). Meanwhile, the ECDA exhibits salty biases more than 0.1 psu from surface to 100 m depth during 1960–1992 (Fig. 18h). This salty bias significantly disappears since 1993 when pseudo salinity profiles are assimilated to the ECDA system. Another salty bias in the western Pacific also significantly decreases since 1993 due to the same reason. Other salinity biases below 400 m of the Atlantic Ocean and overall Indian Ocean gradually decrease in time from the assimilation of Argo data. For the equatorial Pacific, the ECDA shows negative biases more than 0.3 psu along the narrow western boundary areas, and positive biases along the wide thermocline areas, which is the similar feature of the temperature biases. These biases in the ECDA mostly came from those of base model as shown in Fig. 18g and were not completely eliminated

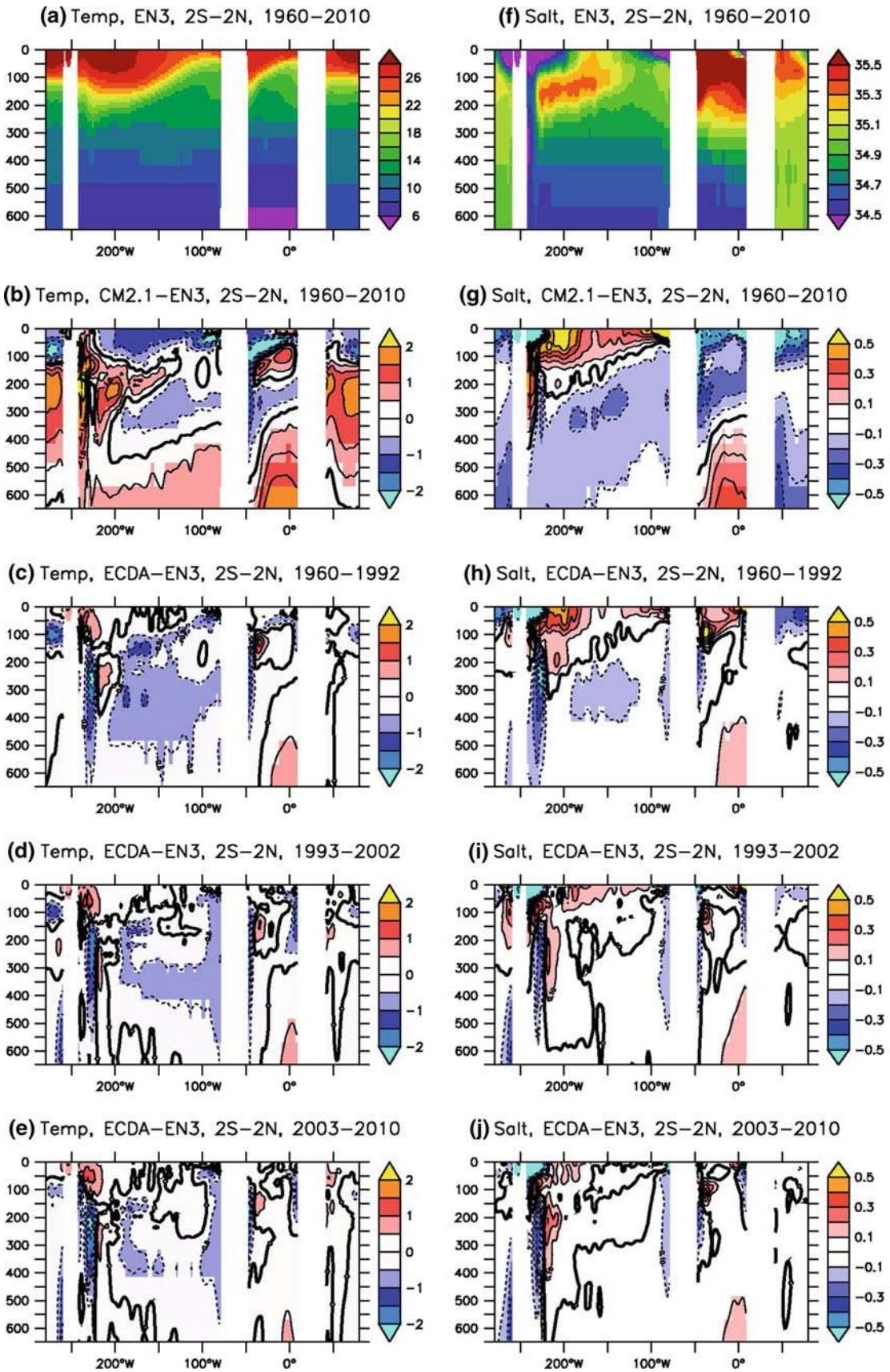
(a) Temp, EN3, 2S–2N, 1960–2010
(f) Salt, EN3, 2S–2N, 1960–2010
(b) Temp, CM2.1–EN3, 2S–2N, 1960–2010
(g) Salt, CM2.1–EN3, 2S–2N, 1960–2010
(c) Temp, ECDA–EN3, 2S–2N, 1960–1992
(h) Salt, ECDA–EN3, 2S–2N, 1960–1992
(d) Temp, ECDA–EN3, 2S–2N, 1993–2002
(i) Salt, ECDA–EN3, 2S–2N, 1993–2002
(e) Temp, ECDA–EN3, 2S–2N, 2003–2010
(j) Salt, ECDA–EN3, 2S–2N, 2003–2010
0
100
200
300
400
500
600
200°W
100°W
0°
26
22
18
14
10
6
35.5
35.3
35.1
34.9
34.7
34.5
2
1
0
−1
−2
0.5
0.3
0.1
−0.1
−0.3
−0.5

◀ **Fig. 18** Average temperature (*left panels*, °C) and salinity (*right panels*, psu) in the 2°S–2°N band for **a**, **f** EN3 for the period 1960–2010, **b**, **g** difference between the CM2.1 and EN3 for the period 1960–1992, **c**, **h** difference between the ECDA and EN3 for the period 1960–1992, **d**, **i** 1993–2002, and **e**, **j** 2003–2010

even after Argo period (Fig. 18j). However, mean biases of the ECDA are relatively small compared to those of CM2.1 and even CFSR (see Fig. 14 from X11). The ECDA also show no temperature and salinity drift in time, while the CFSR experiences significant discontinuity in the deep ocean temperature and salinity of the tropical ocean caused by six data streams during 1979–2009 (see Fig. 15 from X11).

3.6 Major modes of climate variability

In this section, we compare the principal component modes associated with ENSO, IOD, PDO, and AMOC phenomena calculated from the ECDA and observations, respectively. These four major phenomena have strong interannual to decadal variability and have a significant impact on the global climate, so this comparison is very important for accessing the ECDA system. The ECDA serves as an initial condition of the climate prediction model and most climate models experiences model drifts; therefore an assessment on how well the ECDA represents these major modes is necessary. To check any systematic climate drift, note that no trend is applied to most original datasets for the whole analyzed period 1960–2010. For the observations, we used HC300 from the NODC and SSH from the AVISO. As we previously noted, NODC is not exactly independent dataset for the validation of the ECDA, but it is objective analyzed product with a mapping and QC algorithm to make gridded dataset. Moreover, finding enough independent data is impossible when we consider the inhomogeneous of the ocean observing system.

Figure 19 shows that the first two EOFs and PCs of the HC300 from the ECDA are very similar to those from the NODC. The first mode captures the typical El Nino structure (Fig. 19a) and the percent variance calculated by the two datasets (41.7 %) (Fig. 20b), and 42.9 % (Fig. 19c) is also very similar. For the second mode, EOF explains the strong El Nino events especially for 1982–1983 and 1997–1998. The spatial structure from the ECDA shows relatively strong meridional gradient pattern (Fig. 19e) compared to that of NODC (Fig. 19f), but the time series and the variance percentage of the second EOF are similar. It should be noted again that no trend is applied to the original datasets for the whole analyzed period 1960–2010, which indicates that they are robust EOF modes in the tropical Pacific, and they are well represented from both the ECDA and NODC.

For the IOD, we choose SSH instead of HC300 due to large uncertainties from sparse observations around the Indian Ocean before the Argo period. Since a large increasing trend of SSH is also dominant, we remove the linear trend before the EOF calculation. The first EOF pattern of SSH capture the major feature of the dipole mode of thermocline variations with a minimum near Java/Sumatra and a maximum in the south-central Indian Ocean around 10°S (Fig. 20b, c). The largest amplitude of the positive IOD in 1994–1995, 1997–1998, and 2006–2007 are resolved well from both the ECDA and AVISO altimetry (Fig. 20a). However, the variance percentage of the ECDA is larger (39.0 %) than that of the AVISO SSH (26.4 %). Accumulated variance percentage of the first 10th modes is calculated by only 57.0 % from the AVISO observation, while 79.7 % from the ECDA. This difference represents that the quarter degree AVISO observation resolves more independent modes than the ECDA. The second mode explaining 11.9 % of the total variance calculated from the ECDA shows no significant correlation with observations (not shown), so we compare the third mode from the ECDA with the second mode from AVISO. The third (second) EOF mode explains 7.6 % (8.5 %) of the total SSH variance from the ECDA (AVISO), of which common spatial pattern shows the positive anomalies off Java/Sumatra and in the southwestern tropical Indian Ocean and the negative anomalies in the southern Arabian Sea as well as southeastern tropical Indian Ocean (Fig. 20e, f). This spatial pattern is known as quasi-biennial mode (Rao et al. 2002).

Figure 21 shows the first two EOF patterns of HC300 and their corresponding PC time series from the ECDA and NODC in the Northeast Pacific for 1960–2010. The first EOFs from both the ECDA and NODC represent a typical PDO pattern that varies on large decadal time scales and typically lasts for 20–30 years (Mantua et al. 1997). The spatial patterns are very similar (Fig. 21b, c) showing typical structure of the PDO characterized by negative anomalies in the central northeast Pacific flanked by positive anomalies along the west coast of North America, and in the Gulf of Alaska and Bering Sea. As shown in Fig. 21a, PDO cold phase reverses to warm phase around 1977, which is linked to 1976–1977 large-scale climate shift over the Pacific (Miller et al. 1994). After that, short-term flips in PDO phases do occur around 1990–1993 and 2000–2003, and the warm phase seems to be possibly changed to a cold phase since 2007. However, we cannot determine true PDO reversals after 2007 due to a lack of PDO understanding. The phase reversal of PDO could depend on the climatology base period used for EOF calculation. For example, Xue et al. (2011) suggests PDO switched from positive to negative phase around 1999 when they use the 1979–2008 climatology (see Fig 20 from X11).

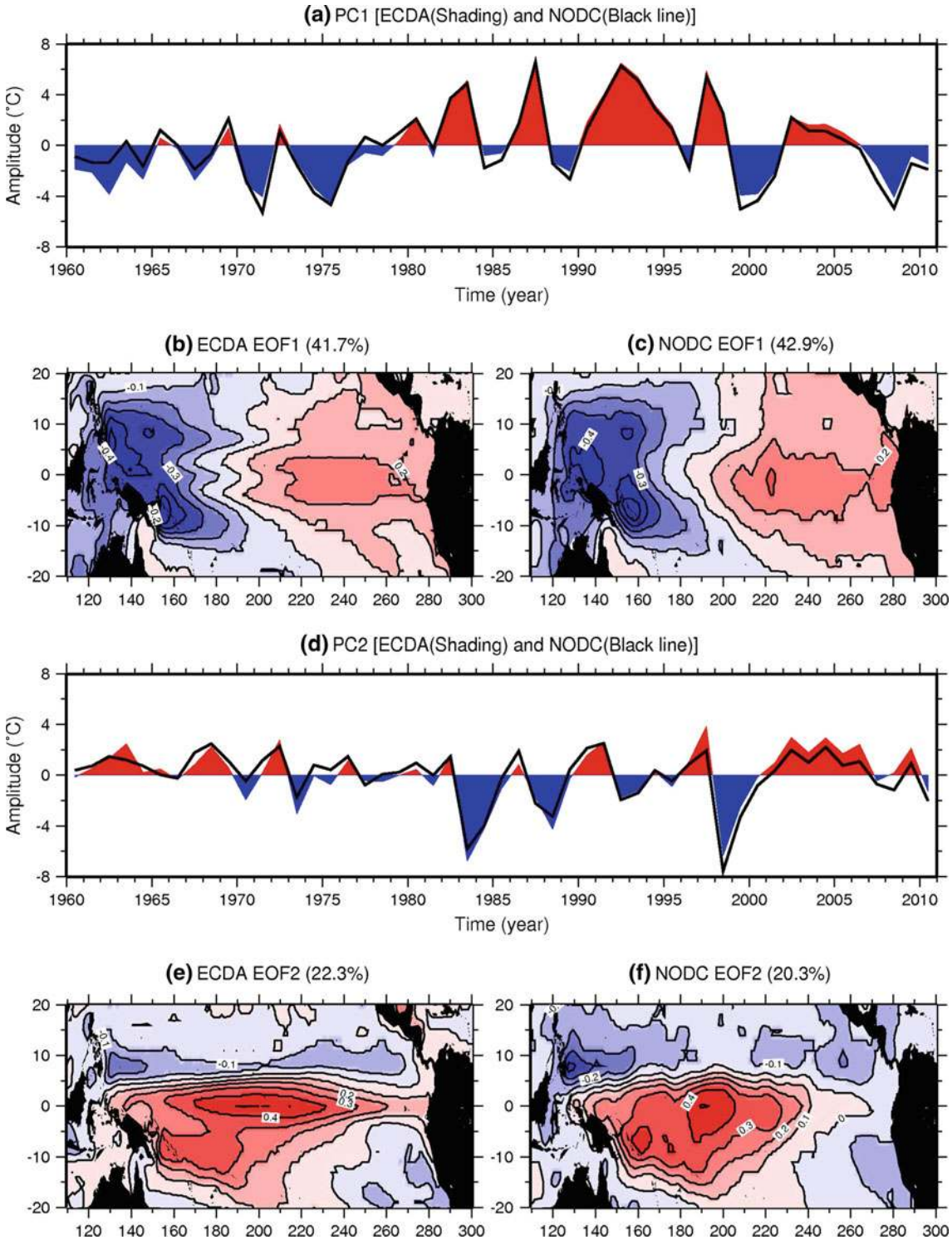

Fig. 19 First two EOFs and PCs of HC300 (°C) anomalies from the ECDA and NODC in the tropical Pacific for the period 1960–2010. For the time series, shading (*black line*) represents the ECDA (NODC). Note that no detrend is applied for the two datasets

Second modes of HC300 from the ECDA and NODC also resemble with each other. Spatial patterns are characterized by a zonal band of negative anomalies between 40°N and 50°N extending southeastward in the subtropical northeast Pacific with positive anomalies in the central Pacific below 40°N (Fig. 21e, f). This spatial pattern is consistent with a dipole structure of the NPGO (North Pacific Gyre Oscillation) (Di Lorenzo et al. 2008), while

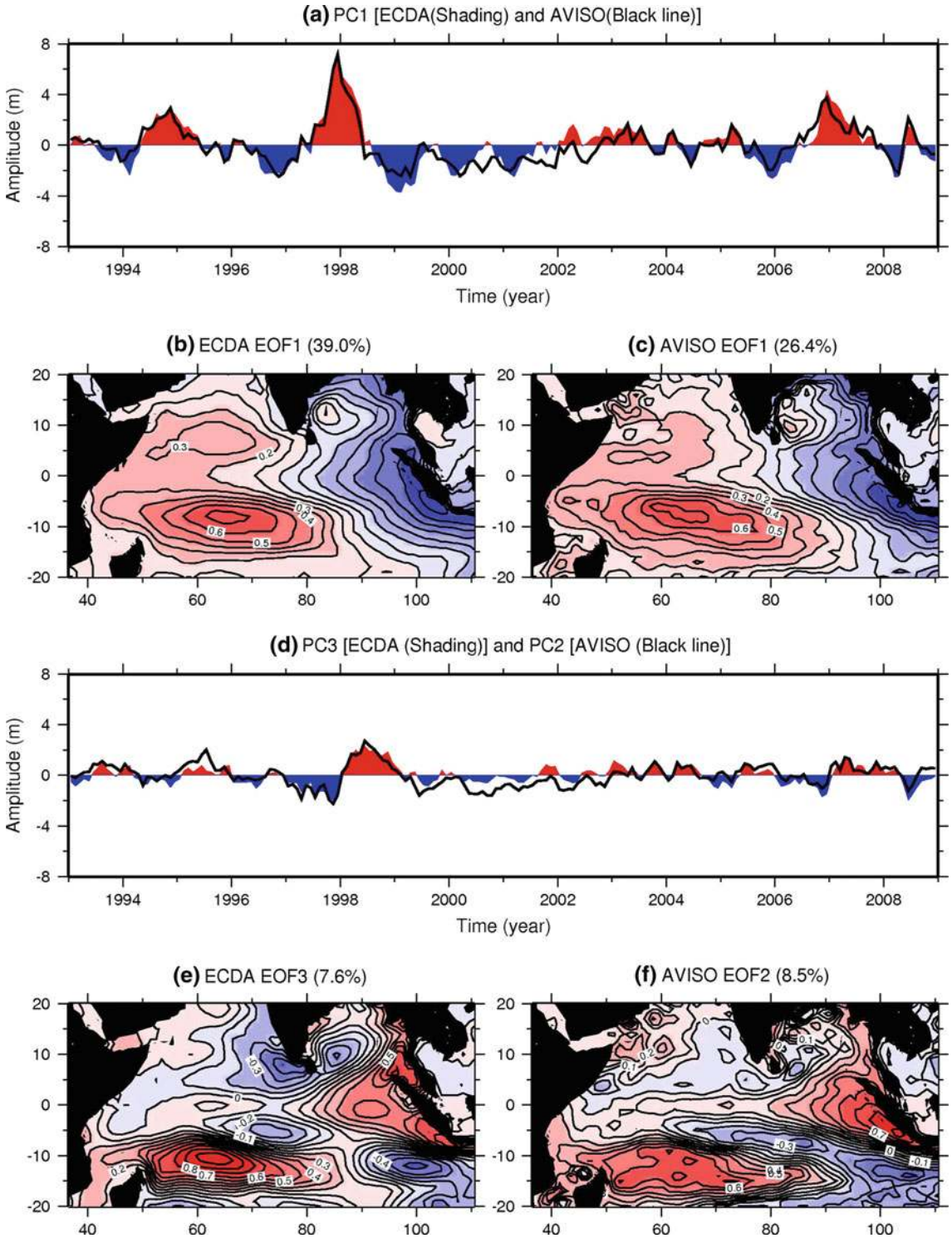

Fig. 20 The same as Fig. 19 except for SSH (cm) anomalies from the ECDA and AVISO in the tropical Indian Ocean for the period 1993–2010. Note that a liner trend has been removed prior to the EOF calculation and EOF3 (PC3) of ECDA are compared to the EOF2 (PC2) of AVISO

two common time series show relatively large amplitudes around 1991–1998 and 1999–2005 (Fig. 21d).

The EOF analysis of HC300 from the ECDA and NODC in the North Atlantic for 1950–2010 also reveals very similar results showing significant long-term and decadal changes associated with the AMOC. The first mode represent a rapid warming trend since 1995 (Fig. 22a), and the warming covers the entire North Atlantic with largest amplitude around the subpolar areas including Labrador and Irminger Seas (Fig. 22b, c). The second mode is

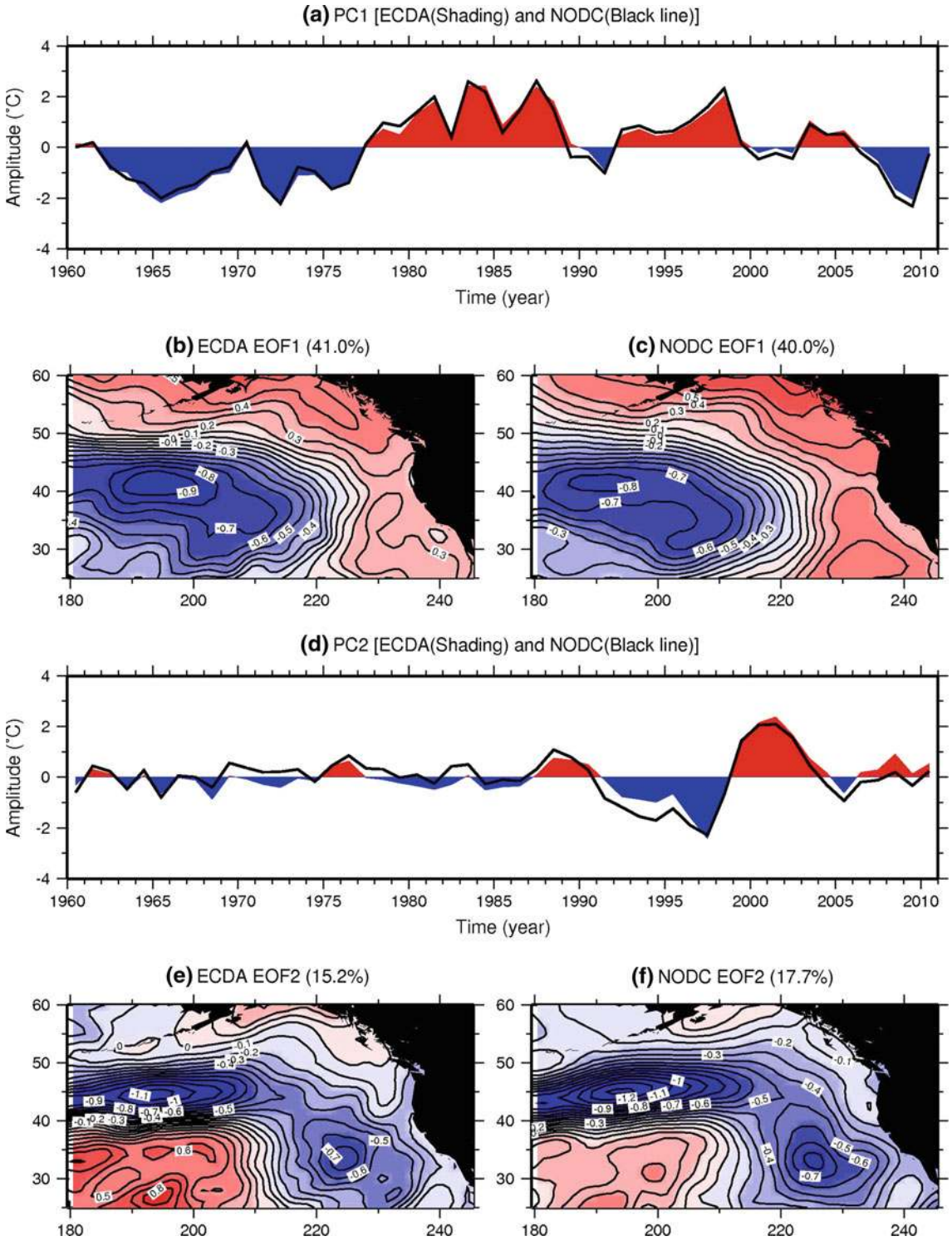

Fig. 21 The same as Fig. 19 except for the North Pacific

characterized by an evident dipole pattern showing the warming in the subtropical gyre with largest amplitude near the Gulf Stream path and cooling in the subpolar gyre. This second mode is similar to the first mode of the altimetry SSH and detrended subsurface temperature at 400 m depth, which is regarded as the fingerprint of the AMOC or Atlantic multidecadal oscillation (Zhang 2008; Mahajan et al. 2011).

For the additional quantitative assessment of the AMOC, we examine the Atlantic overturning transport at 26.5°N where recent RAPID data (Cunningham et al. 2007) are available. One should remember that there are very rare

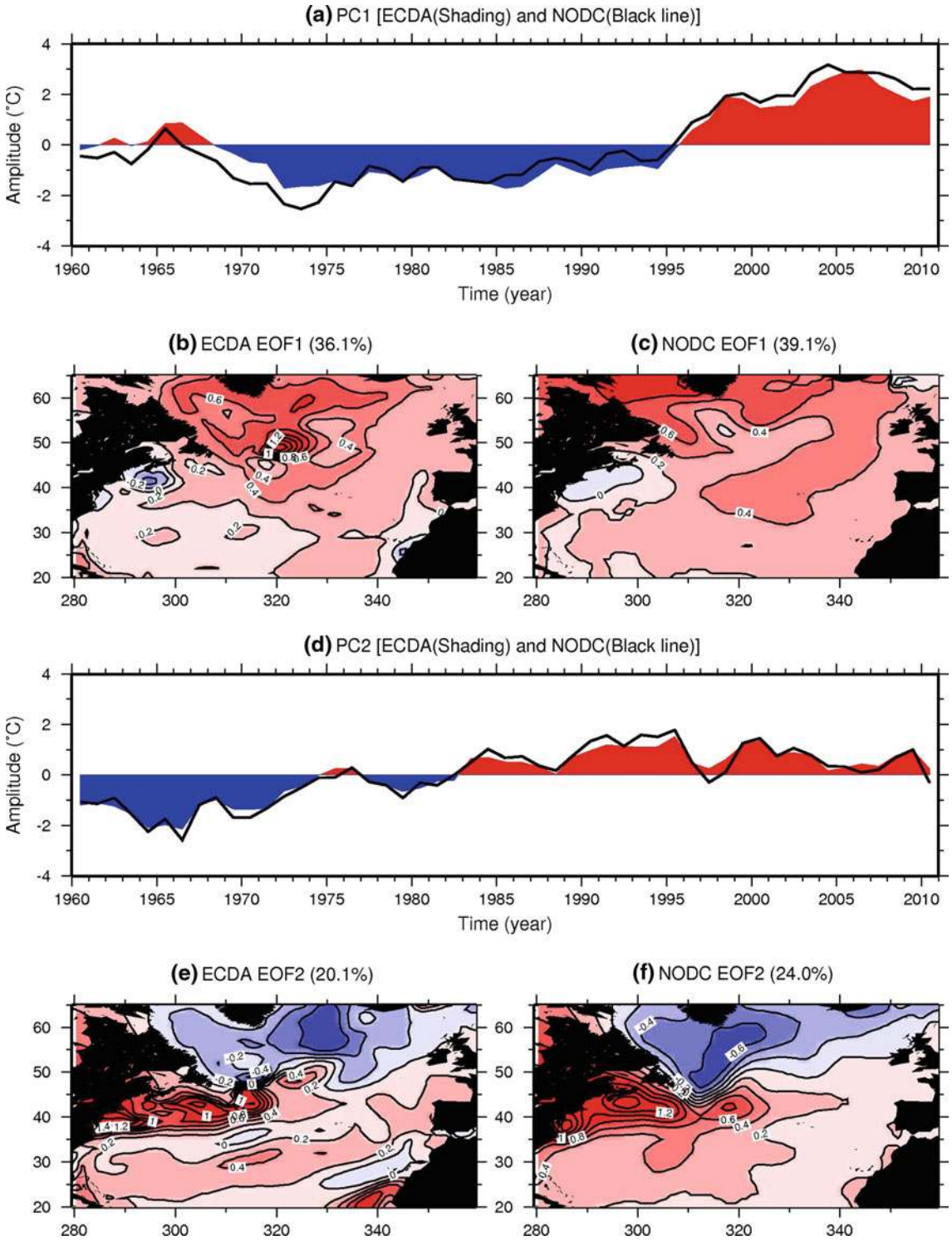

Fig. 22 The same as Fig. 19 except for the North Atlantic

independent observations for the AMOC assessment and likely substantial uncertainties in both the observational estimates and model values. We also expect that more observations below 2,000 m depth help an assimilation system to correctly simulate the AMOC in the future. The AMOC of the ECDA shows prominent variability on seasonal to decadal time scales for 51 years. Mean value of the maximum overturning transport for 51 years is calculated about 12.52 Sv with a standard deviation of 3.22 Sv, which is weaker than that of RAPID data

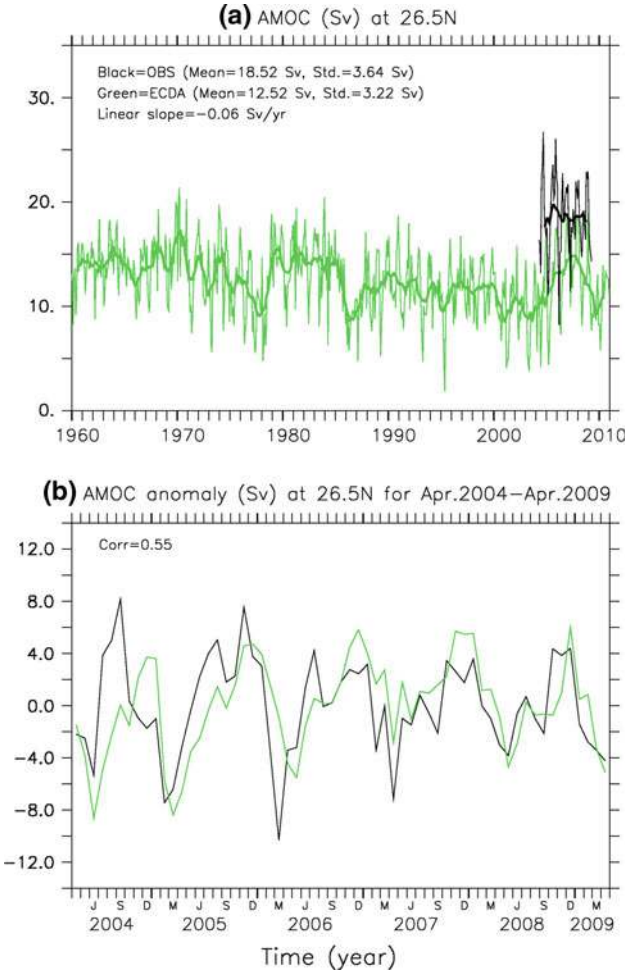

Fig. 23 **a** Time series of the monthly mean of the Atlantic overturning transport at 26.5°N from the (*black lines*) RAPID time series, and (*green lines*) ECDA. *Solid thick lines* are 1-year running mean results. Unit is Sv. **b** Transport anomaly from the (*black lines*) RAPID time series and (*green lines*) ECAD in which their respective means for April 2000–April 2009 are removed

(18.52 ± 3.22 Sv, black line in Fig. 23a) from April 2004 to April 2009. The AMOC of the ECDA also shows a small decrease (−0.06 Sv/year) as well as large interannual variability over the 51 years. This long-term downward trend is consistent with the result from Balmaseda et al. (2007) (−0.07 Sv/year for 1959–2006), but it disagrees with that of Köhl and Stammer (2008) (+0.04 Sv/year for 1952–2001). Figure 23b highlights that the ECDA is able to reproduce fairly well the observed large seasonal cycle with a maximum in summer and a minimum in late winter or early spring. The correlation coefficient between two estimations is calculated at 0.55, which is a little lower than previous results using the GODAS in NCEP (Huang et al. 2012).

In this section, our emphasis is on the similarity between two independent EOF modes from the ECDA and observations rather than providing a detailed physical explanation of individual principal modes. We hope that more detailed analyses on the physical interpretation around these areas will be given by separate studies using other variables generated by the ECDA that are physically related to ENSO, IOD, PDO, and AMOC phenomena.

4 Summary and conclusions

Since the GFDL developed the ECDA system based on a fully coupled climate model with an ensemble Kalman filter (Zhang et al. 2007), there have been several improvements (Zhang and Rosati 2010; Chang et al. 2011b). With the latest version of the ECDA, the GFDL completed the ocean reanalysis for the recent 51 years, 1960–2010. This study informs the user community about the general feature in the ECDA ocean component, and how the ocean reanalysis from the fully coupled model compares with in situ observations and previous reanalyses such as the CFSR developed at the NCEP by using the similar configuration with the companion paper (Xue et al. 2011).

The MHT simulated by the ECDA shows large variability on annual to decal time scales over the 51 years. It is consistent with previous observational estimations within the error ranges during the twentieth century. Significant discrepancy of the MHT between the ECDA and previous estimates is found for the late 1990 and twentieth century especially around the Atlantic Oceans. The surface heat fluxes and wind stress from the ECDA generally agree with observations except for some systematic biases. Compared to the net ocean heat flux from the OAFlux/ISCCP, the ECDA underestimates the warming around the tropics throughout the year, which is consistent with the previous comparisons for the existing reanalysis. For the boreal summer, the ECDA shows cooling bias in the northern oceans and warming bias in the southern oceans, respectively. Imbalance in the mean net heat flux over the global oceans is also found (13.97 W/m^2) in the ECDA, but this imbalance can be shown both in the CFSR (14.7 W/m^2) and observations (30.61 W/m^2).

The wind stress of the ECDA shows stronger trade wind that is related to the warm bias and stronger zonal current in the western equatorial Pacific compared to the TAO and OSCAR data. The westerly wind in the high-latitude southern oceans reveals weakening compared to the existing reanalysis. However, this difference is decreased when we compare with QuickScat SCOW datasets, while existing reanalyses overestimate the strength of the westerly wind in the high-latitude southern oceans. For the equatorial Atlantic Ocean, the ECDA performs better than existing reanalyses in simulation of the zonal wind stress, which is also consistent with better performance of HC300 anomaly around this area.

Compared to the SST and SSS from the WOA09 climatology, the ECDA shows a warm bias in the southern oceans that is related to the systematic CM2.1 model bias. The ECDA's SSS has some biases especially near the river discharge region, but the ECDA well simulates the seasonal change of the SSS, while that of the CFSR is very weak due to a strong nudging to the annual mean SSS climatology. The general features of the MLD climatology are well simulated by the ECDA compared to observation except for an overestimation around the subtropical gyre in northwestern Pacific and Atlantic Oceans, subpolar North Atlantic and high-latitude southern oceans in winter season where deep convection is dominant.

The linear trends of HC300 and SSH from the ECDA show very similar patterns to NODC and AVISO observations. However, the positive trend in the AVISO altimetry is still more prominent around most of oceans especially in the southern oceans, which is related to the discrepancy of the sea level budget shown in previous studies (Willis et al. 2008; Chang et al. 2010; Leuliette and Willis 2011). The ECDA shows good correlation pattern with AVISO around the equatorial Atlantic Ocean, and it increases especially after Argo period. Time series of HC300 around individual ocean basins simulated from the ECDA also agree well with those of observations among three different data sources for the whole analyzed period 1960–2010, when we consider the uncertainties among three different observations.

For the equatorial oceans, the ECDA shows warm difference, stronger surface zonal current, and weaker EUC in the western equatorial Pacific compared to the TAO and OSCAR. By comparing to the CM2.1, we found that underestimated EUC is generated during the assimilation procedure, even though there are substantial improvements for the mean temperature bias, and the variability of zonal current. As for the comparison of the climatology of the temperature and salinity of the ECDA with EN3 data, we find several systematic biases near the surface, thermocline, and boundary area. Some of them disappear with data assimilation procedure, but some remain even after Argo period.

In terms of climate variability, dominant EOF modes of HC300 and SSH calculated from the ECDA represent the main signals associated with ENSO, IDO, PDO, and AMOC. They also agree with those computed from the observation from NODC and AVISO. Seasonal cycle of the AMOC at 26.5°N is well resolved compared to the RAPID data, while the ECDA still underestimates the strength of the maximum northward transport during the recent years.

Acknowledgments We greatly appreciate research groups on OAFlux, ISCCP, ERA40, NODC, TAO, OSCAR, AVISO, EN3, and RAPID for providing their analysis based on observations. The availability of NCEP reanalysis, OISST, WOD09, Argo and GTSPP data also makes the ECDA system possible. We thank R. Msadek and X. Yang for their comments on the earlier version of this manuscript. Suggestions made by two anonymous reviewers were very constructive in the revision of this paper.

References

Anderson JL (2003) A local least squares framework for ensemble filtering. Mon Weather Rev 131:634–642

Antonov JI et al (2010) World Ocean Atlas 2009, volume 2: salinity. In: Levitus S (ed) NOAA Atlas NESDIS 69. U.S. Government Printing Office, Washington, DC 184 pp

Balmaseda MA, Smith GC, Haines K, Anderson D, Palmer TN, Vidard A (2007) Historical reconstruction of the Atlantic Meridional Overturning Circulation from the ECMWF operational ocean reanalysis. Geophys Res Lett 34:L23615. doi:10.1029/2007GL031645

Bonjean F, Lagerloef GSE (2002) Diagnostic model and analysis of the surface currents in the tropical pacific ocean. J Phys Oceanogr 32:2938–2954

Boyer TP et al. (2009) World Ocean Database 2009, Chapter 1: introduction. In: Levitus S (ed) NOAA Atlas NESDIS 66. U.S. Gov. Printing Office, Washington, DC, 216 pp

Boyer TP, Levitus S, Antonov JI, Locarnini RA, Garcia HE (2005) Linear trends of salinity for the World Ocean, 1955–1998. Geophys Res Lett 32:L01604. doi:1029:2004GL021791

Carton JA, Santorelli A (2008) Global upper ocean heat content as viewed in nine analyses. J Clim 21:6015–6035

Chang YS, Rosati A, Zhang S, Harrison MJ (2009) Objective analysis of monthly temperature and salinity for the world ocean in the 21st century: comparison with World Ocean Atlas and application to assimilation validation. J Geophys Res 114:C02014. doi:10.1029/2008JC004970

Chang YS, Rosati A, Vecchi GA (2010) Basin patterns of global sea level changes for 2004–2007. J Mar Syst 80(1–2):115–124. doi:10.1016/j.jmarsys.2009.11.003

Chang YS, Rosati A, Zhang S (2011a) A construction of pseudo salinity profiles for the global ocean: method and evaluation. J Geophys Res 116:C02002. doi:10.1029/2010JC006386

Chang YS, Zhang S, Rosati A (2011b) Improvement of salinity representation in an ensemble coupled data assimilation system using pseudo salinity profiles. Geophys Res Lett 38:L13609. doi:10.1029/2011GL048064

Cunningham SA et al (2007) Temporal variability of the Atlantic meridional overturning circulation at 26.5°N. Science 317:935–938

de Boyer Montégut C, Madec G, Fischer AS, Lazar A, Iudicone D (2004) Mixed layer depth over the global ocean: an examination of profile data and a profile-based climatology. J Geophys Res 109:C12003. doi:10.1029/2004JC002378

Delworth TL et al (2006) GFDL's CM2 global coupled climate model. Part I: formulation and simulation characteristics. J Clim 19:643–674

Delworth TL et al (2012) Simulated climate and climate change in the GFDL CM2.5 high resolution coupled climate model. J Clim 25:2755–2781

Di Lorenzo E et al (2008) North Pacific Gyre Oscillation links ocean climate and ecosystem change. Geophys Res Lett 35:L08607. doi:10.1029/2007GL032838

Ganachaud AS, Wunsch C (2003) Largo-scale ocean heat and freshwater transports during the World Ocean circulation experiment. J Clim 16:696–705

Garzoli SL, Baringer MO (2007) Meridional heat transport determined with expendable bathythermographs, Part II: South Atlantic transport. Deep Sea Res(I) 54(8):1402–1420

Gnanadesikan A et al (2006) GFDL CM2 global coupled climate models, Part II: the baseline ocean simulation. J Clim 19:675–697

Gouretski V, Kiltermann KP (2007) How much is the ocean really warming? Geophys Res Lett 34:L01610. doi:10.1029/2006GL027834

Gouretski V, Reseghetti F (2010) On depth and temperature biases in bathythermograph data: development of a new correction scheme based on analysis of a global ocean database. Deep Sea Res I 57(6):812–834. doi:10.1016/j.dsr.2010.03.011

Griffies SM et al (2005) Formulation of an ocean model for global climate simulations. Ocean Sci 1:45–79

Hakkinen S, Rhines PB (2004) Decline of subpolar North Atlantic circulation during the 1990 s. Science 304:325–340

Hanawa K, Raul P, Bailey R, Sy A, Szabados M (1995) A new depth-time equation for Sippican or TSK T-7, T-6 and T-4 expendable bathythermographs (XBT). Deep Sea Res I 42:1423–1451

Holfort J, Siedler G (2001) The Meridional oceanic transports of heat and nutrients in the South Atlantic. J Phys Oceanogr 31:5–29

Huang RX, Wang W, Liu LL (2006) Decadal variability of wind energy input to the world ocean. Deep Sea Res II 53:31–41

Huang B, Xue Y, Kumar A, Behring DW (2012) AMOC variations in 1979–2008 simulated by NCEP operational ocean data assimilation system. Clim Dyn 38:513–525. doi:10.1007/s00382-011-1035-z

Hunke EC, Dukowicz JK (1997) An elastic-viscous-plastic model for sea ice dynamics. J Phys Oceanogr 27:1849–1867

Ingleby B, Huddleston M (2007) Quality control of ocean temperature and salinity profiles historical and real-time data. J Mar Syst 65:158–175

Ishii M, Kimoto M (2009) Reevaluation of historical ocean heat content variations with time-varying XBT and MBT depth bias corrections. J Oceanogr 65(3):287–299. doi:10.1007/s10872-009-0027-7

Kalnay E et al (1996) The NCEP/NCAR 40-year reanalysis project. Bull Am Met Soc 77:437–471

Kanamitsu M, Ebitsuzaki W, Woolen J, Yang SK, Hnilo JJ, Fiorino M, Potter GL (2002) NCEP-DOE AMIP-II reanalysis (R-2). Bull Am Met Soc 83:1631–1643

Kizu S, Yoritaka H, Hanawa K (2005) A new fall-rate equation for T-5 Expendable Bathythermograph (XBT) by TSK. J Oceanogr 61:115–121

Klein B, Molinari RL, Muller TJ, Siedler G (1995) A trans-atlantic section at 14.5 N: meridional volume and heat fluxes. J Mar Res 53(6):929–957

Köhl A, Stammer D (2008) Variability of the meridional overturning in the North Atlantic from the 50-year GECCO state estimation. J Phys Oceanogr 38:1913–1930. doi:10.1175/2008JPO3775.1

Large WG, Yeager SG (2009) The global climatology of an interannually varying air-sea flux data set. Clim Dyn 33:341–364

Lavin A, Bryden HL, Parrilla G (1998) Meridional transport and heat flux variations in the subtropical North Atlantic. Glob Atmos Ocean Syst 6:269–293

Leuliette EW, Willis JK (2011) Balancing the sea level budget. Oceanography 24(2):122–129. doi:10.5670/oceanog.2011.32

Levitus S, Antonov JI, Boyer TP (2005) Warming of the World Ocean, 1955–2003. Geophys Res Lett 32:L02604. doi:10.1029GL021592

Levitus S, Antonov JI, Boyer TP, Locarnini RA, Garcia HE, Mishonov AV (2009) Global Ocean Heat Content 1955–2008 in light of recently revealed instrumentation problems. Geophys Res Lett 36:L07608. doi:10.1029/2008GL037155

Lin SJ (2004) A "vertically Lagrangian" finite-volume dynamical core for global models. Mon Weather Rev 132:2293–2307

Locarnini RA et al (2010) World Ocean Atlas 2009, volume 1: temperature. In: Levitus S (ed) NOAA Atlas NESDIS 68. U.S. Government Printing Office, Washington, DC, p 184

Lock AP, Brown AR, Bush MR, Martin GM, Smith RNB (2000) A new boundary layer mixing scheme. Part I: scheme description and single-column model tests. Mon Weather Rev 128:3187–3199

Lumpkin R, Sppeer K (2007) Global Ocean meridional overturning. J Phys Oceanogr 37:2550–2562

Macdonald AM (1998) The global ocean circulation: a hydrographic estimate and regional analysis. Prog Oceanogr 41:281–382

Macdonald AM, Wunsch C (1996) An estimate of global ocean circulation and heat fluxes. Nature 382:436–439

Mahajan S, Zhang R, Delworth TL, Zhang S, Rosati A, Chang YS (2011) Predicting Atlantic meridional overturning circulation (AMOC) variations using subsurface and surface fingerprints. Deep Sea Res 58(17–18):1895–1903. doi:10.1016/j.dsr2.2010.10.067

Mantua NJ, Hare SJ, Zhang Y, Wallace JM, Francis RC (1997) A Pacific interdecadal oscillation with impacts on salmon production. Bull Am Met Soc 78:1069–1079

Meehl GA et al (2009) Decadal prediction: can it be skillful? Bull Am Met Soc 90:1467–1485

Miller A, Cayan DR, Barnett TP, Graham NE, Oberhuber JM (1994) The 1976–77 climate shift of the Pacific Ocean. Oceanography 7:21–26

Moorthi S, Suarez MJ (1992) Relaxed Arakawa-Schubert: a parameterization of moist convection for general circulation models. Mon Weather Rev 120:978–1002

Rao SA, Behera SK, Masumoto Y, Yamagata T (2002) Interannual subsurface variability in the tropical Indian Ocean with a special emphasis on the Indian Ocean dipole. Deep Sea Res II 49:1549–1572

Rayner NA et al. (2003) Global analyses of sea surface temperature, sea ice, and night marine air temperature since the late nineteenth century. J Geophys Res 108(D14):4407. doi:10.1029/2002JD002670

Reynolds RW, Chelton DB (2010) Comparisons of daily sea surface temperature analyses for 2007–08. J Clim 23:3545–3562

Reynolds RW, Rayner NA, Smith TM, Stokes DC, Wang W (2002) An improved in situ and satellite SST analysis for climate. J Clim 15:1609–1625

Risien CM, Chelton DB (2008) A global climatology of surface wind and wind stress fields from eight years of QuickSCAT scatterometer data. J Phys Oceanogr 38:2379–2413

Saha S et al (2010) The NCEP climate forecast system reanalysis. Bull Am Met Soc 91:1015–1057

Sato OT, Rossby T (2000) Seasonal and low-frequency variability of the meridional heat flux at 36 N in the North Atlantic. J Phys Oceanogr 30:606–621

Schneider EK, Huang B, Zhu Z, DeWitt DG, Kinter JL III, Kirtman B, Shukla J (1999) Ocean data assimilation, initialization, and predictions of ENSO with a coupled GCM. Mon Weather Rev 127:1187–1207

Smith DM et al (2007) Improved surface temperature prediction for the coming decade from a global climate model. Science 317(5839):796–799. doi:10.1126/science.1139540

Speer KG, Holfort J, Reynard T, Siedler G (1996) South Atlantic heat transport at 11S. In: Wefer G, Berger WH, Siedler G, Webb DJ (eds) The South Atlantic: present and past circulation. Springer, Berlin, pp 105–120

Ssalto/Duacs User Handbook (2008) (M)SLA and (M)ADT Near-Real-time and Delayed-time Products, SALP-DU-P-EA-21065-CLS, Edition 1.9

Sugiura N et al (2008) Development of a 4-dimensional variational coupled data assimilation system for enhanced analysis and prediction of seasonal to interannual climate variations. J Geophys Res 113:C10017. doi:10.1029/2008JC004741

Talley LD (2003) Shallow, intermediate, and deep overturning components of the global heat budget. J Phys Oceanogr 33:530–560

Uppala SM et al (2005) The ERA-40 re-analysis. Q J R Meteor Soc 131:2961–3012. doi:10.1256/qj.04.176

Wang W, Xie P, Yoo SH, Xue Y, Kumar A, Wu X (2011) An assessment of the surface climate in the NCEP Climate Forecast System Reanalysis. Clim Dyn 37(7–8):1601–1620. doi:10.1007/s00382-010-0935-7

Wijffels SE, Willis J, Domingues CM, Barker P, White NJ, Gronell A, Ridgway K, Church JA (2008) Changing expendable bathythermograph fall rates and their impact on estimates of thermosteric sea level rise. J Clim 21:5657–5672

Willis JK, Chambers DP, Nerem RS (2008) Assessing the globally averaged sea level budget on seasonal to interannual timescales. J Geophys Res 113:C06015. doi:10.1029/2007JC004517

Winton M (2000) A reformulated three-layer sea ice model. J Atmos Ocean Tech 17:525–531

Wittenberg AT, Rosati A, Lau N-C, Ploshay JJ (2006) GFDL's CM2 global coupled models. Part III: tropical pacific climate and ENSO. J Clim 19(5):698–722. doi:10.1175/JCLI3631.1

Xue Y, Huang B, Hu ZZ, Kumar A, Wen C, Behringer D (2011) An assessment of oceanic variability in the NCEP climate forecast system reanalysis. Clim Dyn 37(11):2511–2539. doi:10.1007/s00382-010-0954-4

Yang XY, Huang RX, Wang DX (2007) Decadal changes of wind stress over the southern ocean associated with Antarctic ozone depletion. J Clim 20:3395–3410

Yang SC, Keppenne C, Rienecker MR, Kalnay E (2009) Application of coupled bred vectors to seasonal-to-interannual forecasting and ocean data assimilation. J Clim 22:2850–2870

Yu L, Weller RA (2007) Objectively analyzed air-sea heat fluxes (OAFlux) for the global ocean. Bull Am Met Soc 88:527–539

Zhang R (2008) Coherent surface-subsurface fingerprint of the Atlantic meridional overturning circulation. Geophys Res Lett 35:L20705. doi:10.1029/2008GL0354623

Zhang S, Rosati A (2010) An inflated ensemble filter for ocean data assimilation with a biased coupled GCM. Mon Weather Rev 138:3905–3931. doi:10.1175/2010MWR3326.1

Zhang Y, Rossow W, Lacis A, Oinas V, Mishchenko M (2004) Calculation of radiative flux profiles from the surface to top-of-atmosphere based on ISCCP and other global data sets: refinements of the radiative transfer model and input data. J Geophys Res 109:D19105. doi:10.1029/2003JD004457

Zhang S, Harrison MJ, Rosati A, Wittenberg AT (2007) System design and evaluation of coupled ensemble data assimilation for global oceanic climate studies. Mon Weather Rev 135:3541–3564

Zhang S, Rosati A, Harrison MJ (2009) Detection of multidecadal oceanic variability by ocean data assimilation in the context of a "perfect" coupled model. J Geophys Res 114:C12018. doi:10.1029/2008JC005261

Zhang S, Rosati A, Delworth TL (2010) The adequacy of observing systems in monitoring the Atlantic meridional overturning circulation and North Atlantic climate. J Clim 23:5311–5324

Zhang S, Liu Z, Rosati A, Delworth TL (2012) A study of enhancive parameter correction with coupled data assimilation for climate estimation and prediction using a simple coupled model. Tellus A 64:10963. doi:10.3402/tellusa.v64i0.10963